UNIVERSITY OF CALIFORNIA SAN DIEGO

Interfacial Thermal Conductivity/Enhanced Solar Evaporation of Water and Ethanol-Water Mixtures from Porous Media

A dissertation submitted in partial satisfaction of the requirements for

the degree Doctor of Philosophy

in

Engineering Sciences

(Mechanical Engineering)

by

M. Fatih Canbazoglu

Committee in charge:

Professor Prabhakar R. Bandaru , Chair
Professor Jan Kleissl
Professor Yu Qiao
Professor Kalyanasundaram Seshadri
Professor Daniel Tartakovsky

2018

The Dissertation of M. Fatih Canbazoglu is approved, and it is acceptable in quality and form for publication on microfilm and electronically:

Chair

University of California San Diego

2018

DEDICATION

To

My parents,

Aysenur Canbazoglu, Suat Canbazoglu,

and

My brothers,

Omer Canbazoglu, Ibrahim Canbazoglu

TABLE OF CONTENTS

LIST OF ABBREVIATIONS

I.M.: Intrinsic meniscus

E.: Evaporating thin film

N-E: Non-evaporating region

SEM: Scanning electron microscope

TC: Thermocouples

PPI: Pores per inch

CF: Carbon foam

E: Ethanol

W: Water

TBR: Thermal boundary resistance

ETM: Effective thermal medium

int: Interfacial

IR: Infra-red

th: Thickness

LIST OF SYMBOLS

l: Thickness

κ: Thermal conductivity

θ: Rotation angle

R_{int}: Interfacial thermal resistance

q: Heat flux

J: Jacobian

T: Temperature

∅: Heat flux bending angle

P_v: Vapor pressure

μ: Viscosity

σ: Surface tension

ρ: Density

Δm_t: Evaporation rate

h^{evap}: Evaporative heat transfer coefficient

h^{conv}: Convective heat transfer coefficient

η: Efficiency

P_s: Input solar radiation power

P_d: Disjoining pressure

A: Dispersion/Hamaker constant

P_c: Capillary pressure

K: Interfacial curvature

Q: Flow rate

A_s: Surface area

V_s: Flow velocity

Ca: Capillary number

α: Thermal expansion coefficient

V: Volume

C: Specific heat

τ: Thermal time constant

T_{bp}: Boiling point

t_w: Initial waiting time

x_i: Molar fraction

γ: Activity coefficient

Re: Reynolds number

Pr: Prandtl number

H: Enthalpy of evaporation

Q_{heat}: Thermal energy flux

R: Gas constant

Λ: Van Laar Constants

V_m: Molar volume

λ: Interaction energy

LIST OF FIGURES

LIST OF TABLES

ACKNOWLEDGMENTS

First and foremost, I would like to express my sincere appreciation to my advisor Prof. Prabhakar R. Bandaru, for his guidance, strong support and kind help during my PhD study. Without his priceless guidance, my PhD research work wouldn't have been possible. I would also like to thank the other faculty members who have served on my dissertation committee: Prof. Daniel Tartakovsky, Prof. Jan Kleissl, Prof. Yu Qiao and Prof. Kalyanasundaram Seshadri, for their time and their helpful suggestion during the candidate exam.

I would like to thank my friend and colleague Dr. Krishna Vemuri for his help with my experimental work and for his valuable discussions on all my research projects during my PhD.

I would like to extend my gratitude to all my peers in Prof. Bandaru's lab, Dr. Serdar Yavuz, Dr. Cihan Kuru, Dr. Alireza Kargar, Dr. David Moreira, Marcelis Muriel, Hidenori Yamada, Dr. Byung-wook Kim, Dr. Hasan Faraby, Dr. Rahul Kapadia, Dr. Anna Alexander, Anindita Bhattacharya, Zichen Zhang, Peng Chen, Bei Fan, Erick Martinez-Loran, Nirjhar Sarkar, Yun Zhou and Abhishek Satisha, for sharing their knowledge during the weekly group meetings and for their support throughout my PhD.

Chapter 1, in full, has been published in "Estimating interfacial thermal conductivity in metamaterials through heat flux mapping", Applied Physics Letters, 106, 143904 (2015) by M. Fatih Canbazoglu, K. P. Vemuri, P. R. Bandaru. The dissertation author was the primary researcher and author of this material.

Chapter 2, in full, has been published in "Enhanced solar evaporation of water from porous media, through capillary mediated forces and surface treatment", AIP Advances 6,

085218 (2016) by M. Fatih Canbazoglu, B. Fan, A. Kargar, K. Vemuri, and P.R. Bandaru. The dissertation author was the primary researcher and author of this material.

Chapter 3, in full, has been published in "Enhanced solar thermal evaporation of ethanol-water mixtures through the use of porous media", ACS Langmuir 34, 36, 10523-10528 (2018) by M. Fatih Canbazoglu, B. Fan, K. Vemuri, and P.R. Bandaru. The dissertation author was the primary researcher and author of this material.

VITA

2009 BS, Mechanical Engineering, Yildiz Technical University, Turkey

2012 MS, Engineering Sciences (Mechanical Engineering), University of California San Diego

2018 PhD, Engineering Sciences (Mechanical Engineering), University of California San Diego

PUBLICATIONS

1. K. P. Vemuri, F. M. Canbazoglu, P. R. Bandaru, "Guiding conductive heat flux through thermal metamaterials", Applied Physics Letters, 105, 193904 (2014).
2. K. P. Vemuri, F. M. Canbazoglu, P. R. Bandaru, "Experimental verification of heat flux bending in multilayered thermal metamaterials", Metamaterials: Fundamentals and applications 9160, 916010 (2014).
3. M. Fatih Canbazoglu, K. P. Vemuri, P. R. Bandaru, "Estimating interfacial thermal conductivity in metamaterials through heat flux mapping", Applied Physics Letters, 106, 143904 (2015).
4. P. R. Bandaru, K.P. Vemuri, M. Fatih Canbazoglu, R. S. Kapadia, "Layered thermal metamaterials for the directing and harvesting of conductive heat", AIP Advances 5, 053403 (2015).
5. M. Fatih Canbazoglu, B. Fan, A. Kargar, K. Vemuri, and P.R. Bandaru, "Enhanced solar evaporation of water from porous media, through capillary mediated forces and surface treatment", AIP Advances 6, 085218 (2016).

6. M. Fatih Canbazoglu, B. Fan, K. Vemuri, and P.R. Bandaru, “Enhanced solar thermal evaporation of ethanol-water mixtures through the use of porous media”, ACS Langmuir 34, 36, 10523-10528 (2018).

ABSTRACT OF THE DISSERTATION

Interfacial Thermal Conductivity/Enhanced Solar Evaporation of Water and Ethanol-Water Mixtures from Porous Media

by

M. Fatih Canbazoglu

Doctor of Philosophy in Engineering Sciences (Mechanical Engineering)

University of California San Diego, 2018

Professor Prabhakar R. Bandaru, Chair

Interfaces are recognized as being one of the biggest impediments to efficient heat transfer, and interfacial effects tend to dominate heat transfer processes between disparate materials. Despite this, not a great deal of research had been done on exactly how interfaces alter the direction and quality of heat flux on metamaterials, as they had been treated as an effective medium. The aim of the first project was to investigate the variability of the thickness as well as the thermal conductivity of interfaces in composites which may significantly influence thermal transport characteristics and the notion of a metamaterial as an effective medium. The consequent modulations of the heat flux passage are analytically and experimentally examined through a non-contact methodology using radiative imaging, on a model anisotropic thermal metamaterial. It was indicated that a lower Al layer/silver interfacial epoxy ratio of ~25 compared to that of a Al layer/alumina interfacial epoxy (of ~39) contributes to a smaller

deviation of the heat flux bending angle. Another major finding was that the role of interfacial conductivity variation was much more significant in altering the heat flux bending angle than that of the interface thickness variation.

Solar irradiation is a valuable source of renewable energy. In fact, the hourly incident solar flux on the surface of the earth is greater than the planet's annual global energy consumption. In the second project, solar steam generation on carbon foam samples was investigated and solar thermal efficiency of around 60% was achieved. The goal of the project was to examine the effects of three specific parameters known to affect efficiency: pore size and distribution, the relative contribution of conductive and convective heat transfer, and the constitution and characteristics of the materials used in the porous media and related chemistry. One of the chief findings was that evaporation efficiency was boosted by decreased pore size. Furthermore, it was also determined that the chemical modification of surfaces increases capillary pressure. Heat transfer coefficient values through the analysis of the heat transfer mechanism on the carbon foam top surface were also investigated and it was found that heat transfer coefficient values increase with reduced pore size.

Carbon foam based porous media is used to examine water, and ethanol-water mixtures evaporation as well for the third project. A relationship between the consequent rate of mass loss, with respect to the equilibrium vapor pressure, dynamic viscosity, surface tension, and density, was developed to explain experimental observations. The evaporative heat loss was parameterized through two convective heat transfer coefficients – one related to the surface and another related to the vapor external to the surface. The work promotes a better understanding of thermal processes in binary liquid mixtures with applications ranging from phase separation to distillation and desalination.

CHAPTER 1: ESTIMATING INTERFACIAL THERMAL CONDUCTIVITY IN METAMATERIALS THROUGH HEAT FLUX MAPPING

1.1 Introduction

Metamaterials are often synthesized through optimized arrangement or layering of isotropic materials and should ideally can be treated as an effective medium [1,2]. Such a requirement intrinsically assumes that the interfaces between the constituents are not relevant in determining the overall characteristics of the metamaterial. For example, a wavelength/structural feature ratio of 10:1 has often been considered [3] as one criterion for an effective medium in the case of electromagnetic interactions. However, for the case of diffusive transport [4], as would be the case for thermal metamaterials, the criterion is less well defined [5]. In this paper, we consider the possible effects of interfaces in modulating heat transfer [6,7] in thermal metamaterials. We use a novel non-contact methodology, based on radiative heat imaging, for probing the role of the interfacial thickness as well as its thermal conductivity in regulating the heat flux through composite media [8].

At the very outset, the interfacial thermal resistance [9] (R_{int}) is defined for an area, A, through: $R_{int}A = l_{int}/\kappa_{int}$, where l_{int} and κ_{int} are the effective thickness and thermal conductivity of the interface, respectively: Fig. 1.1 (a). In practical construction of the composite, there is an intrinsic variability in both the l_{int} and the κ_{int}, and could play a major role in establishing a true metric of the thermal boundary resistance (TBR) [10]. We seek to understand the modulation of a specific functionality in thermal metamaterials [5,11], *i.e.,* the variation of the heat flux bending, due to such physical parameter fluctuations intrinsic to an interface.

1.2 Interfacial heat flux bending angle

We have previously shown [5] that assembling a composite of two alternating materials of the same thickness, with isotropic thermal conductivity (of κ_1 and κ_2, say, with $\kappa_1 > \kappa_2$: Fig. 1.1(a), and rotating the layers (say, by an angle θ as in Fig. 1.1(b)), with respect to a horizontal thermal gradient direction may cause the heat flux to bend by a specific angle: ϕ. In the earlier treatment [5], the interfacial effect was completely ignored under a proposed effective thermal medium (ETM) approach. It was approximated here that the difference (ΔT) between the temperatures obtained at a given point - (i) obtained through assuming a linear temperature gradient across the composite (equivalent to defining an effective thermal conductivity for the composite) and (ii) through considering temperature variation across the individual layers, could be drastically reduced, through a large κ_1 / κ_2 ratio as well as a large number of layers (n) in the composite. Consequently, the angle of heat flux bending could be derived as:

$$\phi = \mathrm{Tan}^{-1}\left[\frac{(-1+c)\cos(\theta)\sin(\theta)}{\cos^2(\theta)+c\,\sin^2(\theta)}\right], \text{ with } \; c = \frac{\left(1+\kappa_1/\kappa_2\right)^2}{4\,\kappa_1/\kappa_2} \tag{1.1}$$

Both positive and negative values of the ϕ corresponding to the upwards/downwards bending of the heat flux was also demonstrated [12]. However, in the earlier study, (a) the two layers were assumed to be of equal thickness, and (b) interfacial effects were ignored. As an example of the construction of an ETM, we now consider a composite constituted from Al layers ($\kappa_1 = \kappa_{Al}$) joined together with epoxy ($\kappa_2 = \kappa_{int}$), which serves as the interfacial (*int*) material. When both l_{int} and κ_{int} are considered the heat flux bending angle would be modified to ϕ_{int} (see Section A1. of the Appendix for further details of the derivation), to a value:

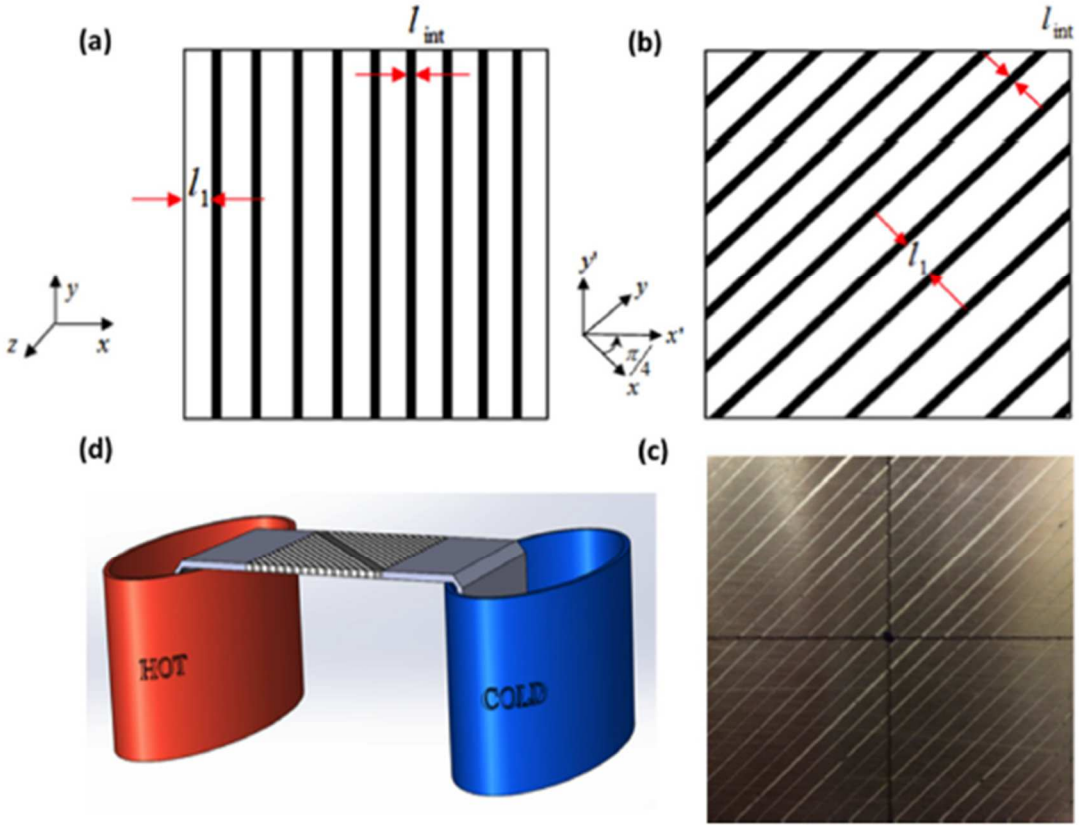

Figure 1.1: (a) A multilayered composite/metamaterial may be fabricated through joining isotropic material (of thickness: l_1 and thermal conductivity: κ_1) and an interfacial epoxy (of thickness: l_{int} and thermal conductivity: κ_{int}), **(b)** Anisotropy can be induced in the composite through rotating the layers of the composite by an angle θ, leading to a heat flux bending, which would be sensitive to the l_{int} and κ_{int}, **(c)** An experimental sample composed of Aluminum layers joined by epoxy , with the layers oriented at θ=45°, **(d)** The composite sample was placed in a temperature gradient (~80 K sustained over a length of ~ 9 cm), facilitated through hot and cold water both reservoirs.

$$\phi_{\text{int}} = \text{Tan}^{-1}\left[\frac{(-a+b)\cos(\theta)\sin(\theta)}{a\cos^2(\theta) + b\sin^2(\theta)}\right]$$

$$a = \left(l_{Al} + l_{\text{int}}\right)^2\left(\frac{\kappa_{Al}}{\kappa_{\text{int}}}\right), b = \left(\frac{\kappa_{Al}}{\kappa_{\text{int}}}\right)l_{Al}^2 + \left(\frac{\kappa_{Al}}{\kappa_{\text{int}}}\right)^2 l_{Al}l_{\text{int}} + l_{Al}l_{\text{int}} + \left(\frac{\kappa_{Al}}{\kappa_{\text{int}}}\right)l_{\text{int}}^2 \quad (1.2)$$

It is evident then that the presence and consideration of the interface significantly alters the heat flux bending angle. Consequently, the experimental observation of the heat flux could yield

insights into the interfacial characteristics.

1.3 Experimental

The experiments were carried out through assembling an even number (n=34) of thin layers of Aluminum (assuming an isotropic κ_{Al}=205 W/mK, and l_{Al} = 0.17 cm) which were joined together using two different types of thermally conductive adhesive, *i.e.,* (i) an alumina epoxy (from Arctic Silver, Inc., specified by the manufacturer with a thermal conductivity in the range of 0.5 to 7.5 W/mK), and (ii) a silver epoxy (Arctic Silver, Inc., specified with a thermal conductivity > 7.5 W/mK), respectively: Fig. 1.1(b) and 1.1(c). The samples were fabricated in a square geometry with a length and width of 5 cm each, and have a thickness of ~ 0.3 cm, implying a large length/width to thickness aspect ratio (of ~ 17) and the treatment of the heat flux in a two-dimensional ETM plane. The assembly process naturally incorporates variability in both the l_{int} and κ_{int}, with the interface consisting of the joining epoxy. The metamaterial assembly was oriented at an angle θ = 45^o, as indicated in Fig. 1.1(c), with respect to a horizontal temperature gradient of ~ 80 K (T_{hot} = 100 ^{o}C, and T_{cold} = 22 ^{o}C): Fig. 1.1(d). The hot and cold-temperatures were maintained using water baths of large heat capacity. The steady state temperature profiles were obtained through using an infra-red (IR) camera (FLIR 320), with a spatial resolution/spot size of ~ 385 μm and a temperature resolution of ~ 0.5 K . For obtaining an enhanced signal, the top surfaces of the samples of Fig. 1.1(c) were painted with a thin layer of black paint (of emissivity 0.95).

1.3 Results and Discussion

The results of the imaging are indicated through the temperature recordings in Fig. 1.2(a) - for the silver epoxy, and Fig. 1.2(b) - for the alumina epoxy. While the heat flux lines would

not be oriented in the temperature gradient direction, due to the anistropy in the composite/metamaterial, the bending of the flux is still evident in the considered figures. Given that the typical interface thickness to the Al layer thickness ratio was determined to be of the order of 0.1 (as also discussed later with reference to Fig. 1.3), it is remarkable that a considerable heat flux modulation is being observed. The relative spacing of the isotherms in the

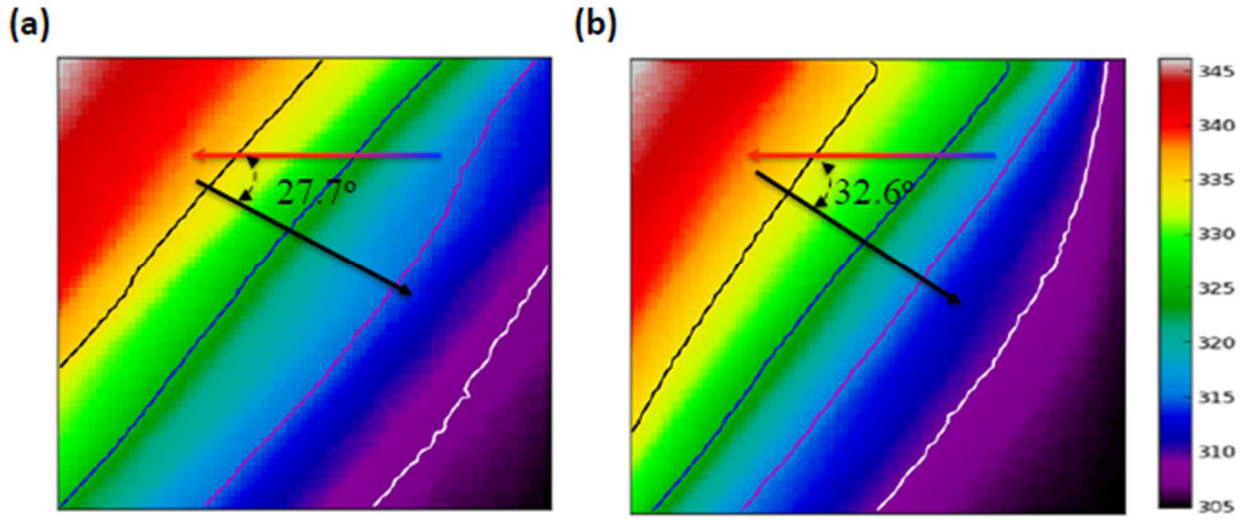

Figure 1.2: The steady state transport of heat, as obtained by infra-red imaging, through **(a)** aluminum layer-silver epoxy, and **(b)** aluminum layer-alumina epoxy, joined composites. The scale bar indicates the temperatures. Typical isothermal contours are at 335 K, 325 K, 315 K, and 308 K, from the left to right. The angles refer to the direction of *net* heat flux bending with respect to a horizontally applied temperature gradient.

composite would be a function of the κ_{Al}/κ_{int} ratio, and may be understood by reference to a limiting case where an extremely large material/interface thermal conductivity ratio could yield a situation where further compression of the isotherms towards the center of the composite would occur.

The spot size enabled by the IR camera yielded a matrix (130 X 130 points) of temperature readings : $T(x,y)$ over the sample area. At steady state and in the absence of losses, the heat conduction equation for a given heat flux q_i in the anisotropic composite, would be:

$$\nabla \cdot q_i = \nabla \cdot \left(\kappa_{ij} \nabla T_j \right) = \kappa_{xx} \frac{\partial^2 T(x,y)}{\partial x^2} + \kappa_{xy} \frac{\partial^2 T(x,y)}{\partial x \partial y} + \kappa_{yy} \frac{\partial^2 T(x,y)}{\partial y^2} = 0 \qquad (1.3)$$

In the above relation, the κ_{xx}, κ_{xy}, and κ_{yy} are all functions of the κ_{Al}, l_{Al}, κ_{int}, l_{int}, and the θ (see Appendix). As all the other variables, except the l_{int} or the κ_{int} are known, the solution of Eqn. (1.3) would determine the interfacial characteristics.

Initially, the horizontal and vertical temperature gradients were obtained through averaging the temperature readings over a length of 5 points. Such a distance of 0.1925 cm (= 385 μm X 5) was chosen to ensure that the interface between the Al layers was always sampled, *i.e.,* as the l_{Al} = 0.17 cm. Subsequently, the second derivatives: $\frac{\partial^2 T(x,y)}{\partial x^2}$, $\frac{\partial^2 T(x,y)}{\partial y^2}$, and $\frac{\partial^2 T(x,y)}{\partial x \partial y} \left(= \frac{\partial^2 T(x,y)}{\partial y \partial x} \right)$ were computed through a second-order forward difference methodology (also see Section A2. of the Appendix).

Then, the location of each interface, on the line transverse to that along which the temperatures were recorded, and the corresponding l_{int} were measured through scanning electron microscopy (SEM) based imaging. A representative variation of the l_{int} is indicated for ten consecutive interfaces in Fig. 1.3(a) and Fig. 1.3(b), for the Al layers joined by alumina and silver epoxy. It was noted that the $l_{int,\ alumina}$ was 203 ± 81 μm and the $l_{int,\ silver}$ was 209 ± 114 μm, respectively. Subsequently, Eqn. (1.3) was solved, considering the interfaces imaged through the SEM and using the l_{int} values to yield the $\kappa_{int.}$ The variation of the $\kappa_{int,\ alumina}$ along the ten interfaces is indicated in Fig. 1.3(c) – with a range of 3.0-7.3 W/mK (averaged as 5.2 ±

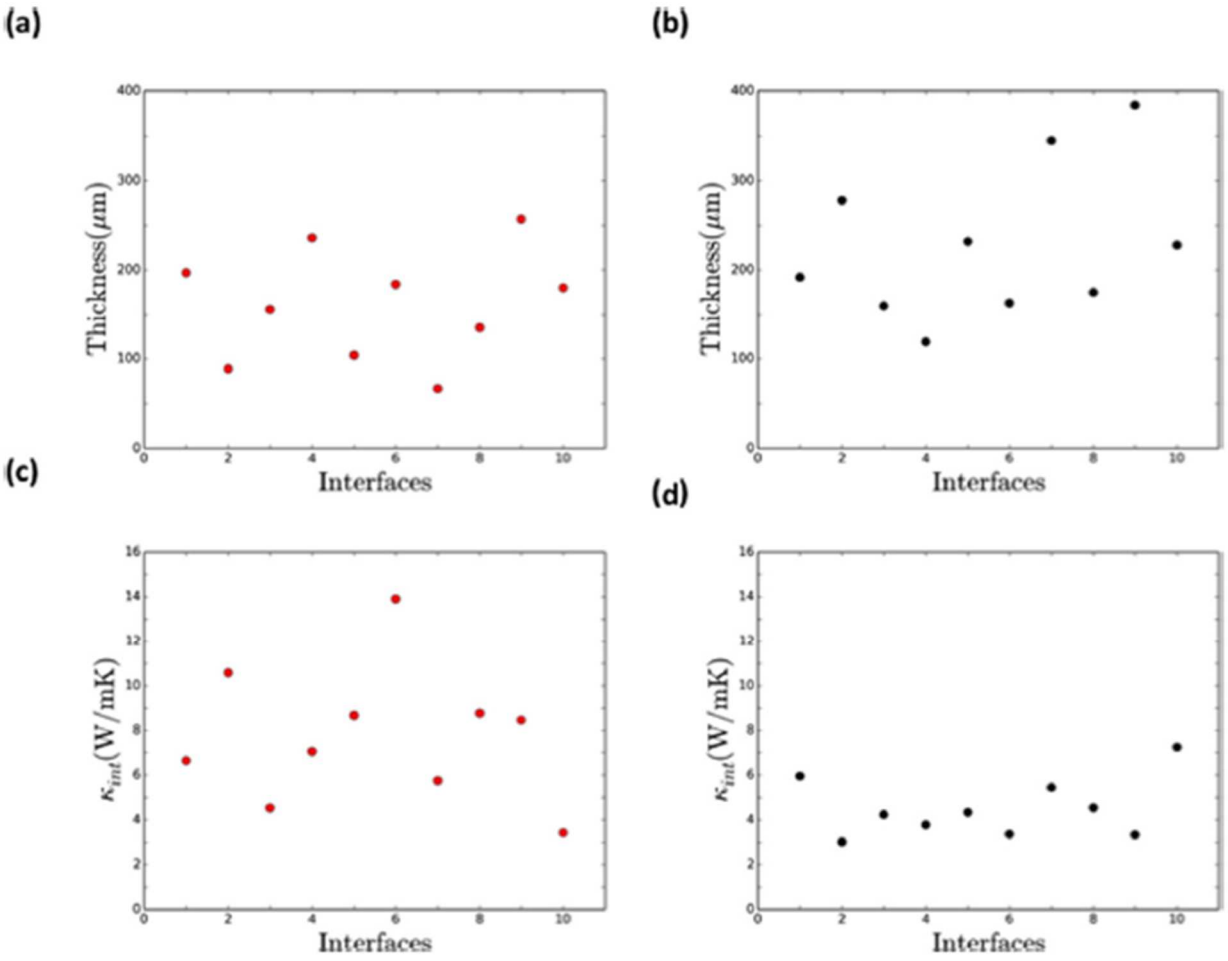

Figure 1.3: The measured interfacial thickness variation, for the **(a)** aluminum layer-silver epoxy, and **(b)** aluminum layer-alumina epoxy, joined composites. The estimated thermal conductivity variation for the **(c)** aluminum layer-silver epoxy, and **(d)** aluminum layer-alumina epoxy, joined composites.

3.7 W/mK), and that for $\kappa_{int,\ silver}$ in Fig. 1.3(d) – with a range of 3.4-13.9 W/mK (averaged to be 8.3 ± 3.4 W/mK). Such variation in both the l_{int} and the κ_{int} is representative of practical interfaces, and the latter is be contrasted to typical manufacturer specifications of the epoxy thermal conductivity (*i.e.,* 0.5-7.5 W/mK for the alumina epoxy and > 7.5 W/mK for the silver epoxy). The estimates of the interfacial resistance [13,14,7], $R_{int}A$ (= l_{int}/κ_{int}) range from (0.3-13.4) × 10^{-5} m^2K/W and (1.0- 4.4) × 10^{-5} m^2K/W, for the Al layer-alumina epoxy and the Al layer-silver epoxy constituted composites, respectively.

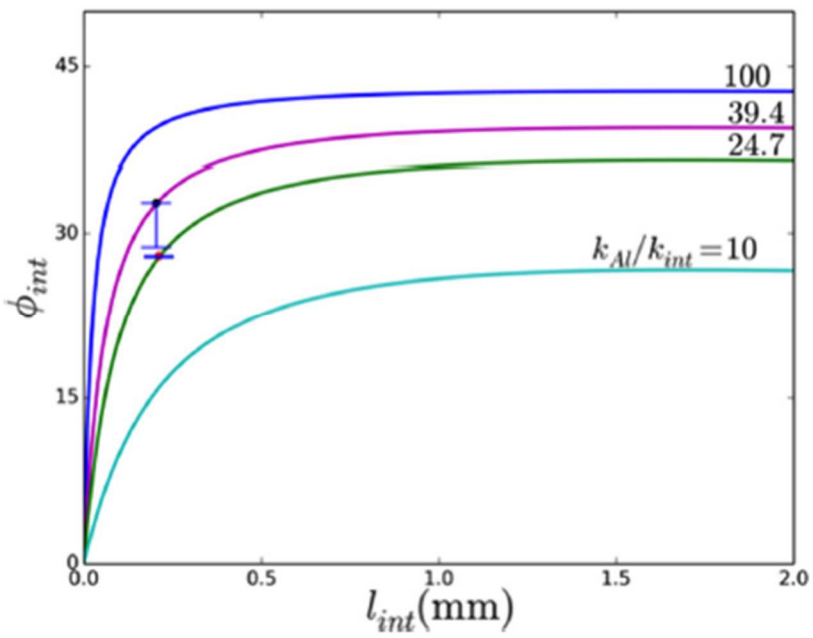

Figure 1.4: The heat flux bending angle ($\emptyset_{int}$ variation with the interfacial thickness (l_{int}) as a function of the κ_{Al}/κ_{int} ratio, plotted per Eqn. (1.2) and with θ=45°. The marked points correspond to the determined $\kappa_{Al}/\kappa_{int,\ alumina}$ ratio of ~ 39.4 and a $\kappa_{Al}/\kappa_{int,\ silver}$ ratio of ~ 24.7.

For obtaining the average values of the interfacial parameters, Eqn. (1.2) was used to plot the ϕ_{int} as a function of the l_{int} and is shown in Fig. 1.4, with individual curves in the graph correspond to varying κ_{Al}/κ_{int} values. Generally, the ϕ_{int} shows an initial linear variation followed by a saturation behavior at larger values of the l_{int}. Intuitively, large l_{int} corresponds to a situation where the heat flux preferentially follows the higher thermal conductivity Al layer, and a concomitant decreasing influence of the interface. Equivalently, a similar behavior would be expected for a very large κ_{Al}/κ_{int} ratio, and the ϕ_{int} would saturate at an angle of (90-θ) [5]. From κ_{Al} = 205 W/mK, and the obtained average values of the $\kappa_{int,\ alumina}$ and the $\kappa_{int,\ silver}$ (5.2 W/mK and 8.3 W/mK, respectively), the ϕ_{int} was estimated to be 32.6^0 and 27.7^0, for the two adhesives. These values are superposed on the plots of Fig. 1.4 with a $\kappa_{Al}/\kappa_{int,\ alumina}$ ratio of ~ 39.4 and a

κ_{Al} / $\kappa_{int,\ silver}$ ratio of ~ 24.7. These angles correspond to the extent of heat flux bending given through the ϕ_{int} and consider the interfacial effects and variations.

The change in the ϕ_{int} (= $d\phi_{\text{int}}$) due to the variation in the l_{int} (= ∂l_{int}) and the κ_{int} (= $\partial \kappa_{\text{int}}$) can be understood through a relation of the form:

$$d\phi_{\text{int}} = \frac{\partial \phi_{\text{int}}}{\partial \kappa_{\text{int}}} d\kappa_{\text{int}} + \frac{\partial \phi_{\text{int}}}{\partial l_{\text{int}}} dl_{\text{int}} \tag{1.4}$$

Table 1.1: The net change of the observed heat flux bending angle (= $d\phi_{\text{int}}$) due to the individual variation in the interfacial thickness (= ∂l_{int}) and the interfacial thermal conductivity (= $\partial \kappa_{\text{int}}$) for the aluminum layer-silver epoxy, and aluminum layer-alumina epoxy, joined composites.

	$\frac{\partial \phi_{\text{int}}}{\partial \kappa_{\text{int}}}$	$d\kappa_{\text{int}}$ (W/m K)	$\frac{\partial \phi_{\text{int}}}{\partial l_{\text{int}}}$	dl_{int} (μm)	$d\phi_{\text{int}}$
Al-silver epoxy	−1.5	3.4	41.8	114	-0.3^0
Al-alumina epoxy	−1.9	3.7	36.3	81	-4.1^0

The partial derivatives were computed from Eqn. (1.2) and the results of the estimation, with respect to the variation of the heat flux bending angle are indicated in Table 1.1. It is apparent that a higher $\kappa_{Al/}\kappa_{int,silver}$ ratio of ~ 39 compared to the of $\kappa_{Al/}\kappa_{int,alumina}$ of ~ 25, contributes to the smaller deviation of the heat flux bending angle. It is also pertinent to note that the interfacial conductivity variation may play a larger role compared to the thickness variation, due to the dominance of the first term in Eqn. (1.4). As there would always be such thickness and thermal conductivity variation, the degree to which a thermal metamaterial can be approximated as an effective thermal medium should be carefully considered.

1.4 Conclusion

In summary, our work has indicated that considering the variation of the interfacial parameters is crucial for composite and metamaterial layers joined by adhesives with a large $\kappa_{material}/\kappa_{adhesive}$ ratio. We have proposed a non-contact method, based on the amount of heat flux bending that may be used to deduce the interface characteristics, which induce non-idealities and deviations from the predicted values.

Chapter 1, in full, has been published in "Estimating interfacial thermal conductivity in metamaterials through heat flux mapping", Applied Physics Letters, 106, 143904 (2015) by M. Fatih Canbazoglu, K. P. Vemuri, P. R. Bandaru. The dissertation author was the primary researcher and author of this material.

1.5 Appendix

A1. For two-dimensional heat transfer (with a large length/width to thickness ratio):

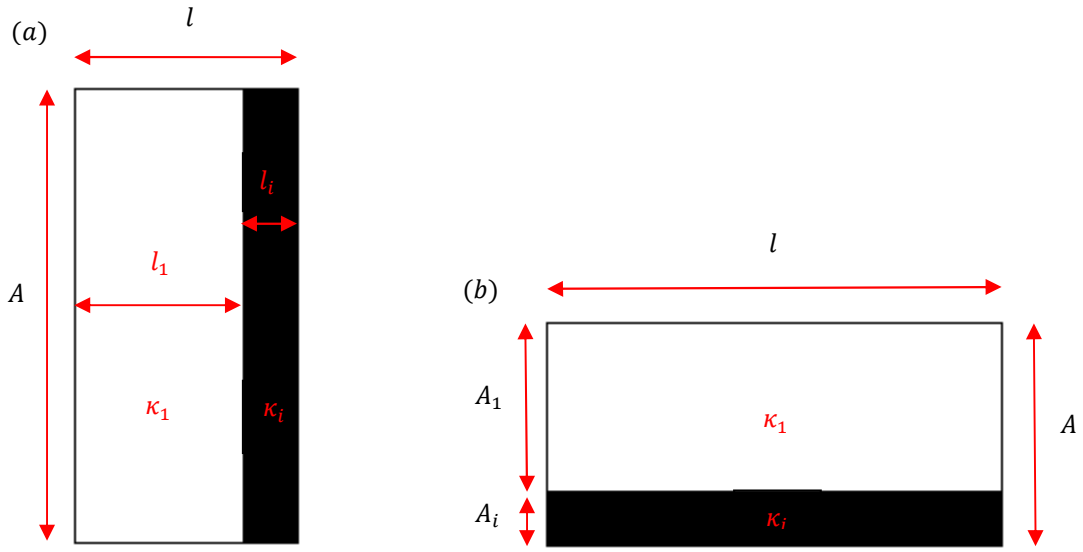

Figure A1.1: The (a) series and (b) parallel configuration of a layered composite constituted from an isotropic material (light) and interfacial epoxy (dark).

SERIES

$$q_1 = q_2 = q$$

$$\kappa_{series} = \frac{(l_1 + l_i)\kappa_1\kappa_i}{l_1\kappa_i + l_i\kappa_1}$$

PARALLEL

$$\nabla T_1 = \nabla T_2 = \nabla T$$

$$\kappa_{parallel} = \frac{\kappa_1 A_1 + \kappa_i A_i}{A_1 + A_i} = \frac{\kappa_1 l_1 + \kappa_i l_i}{l_1 + l_i}$$

The anisotropic thermal conductivity tensor for the composite is then:

$$\kappa_{ij} = \begin{pmatrix} \kappa_x & 0 & 0 \\ 0 & \kappa_y & 0 \\ 0 & 0 & \kappa_z \end{pmatrix} = \begin{pmatrix} \frac{(l_1 + l_i)\kappa_1\kappa_i}{l_1\kappa_i + l_i\kappa_1} & 0 & 0 \\ 0 & \frac{\kappa_1 l_1 + \kappa_i l_i}{l_1 + l_i} & 0 \\ 0 & 0 & \frac{\kappa_1 l_1 + \kappa_i l_i}{l_1 + l_i} \end{pmatrix} \quad \text{(A1.1)}$$

However, due to the lack of off-diagonal κ_{ij} components, there is no bending of heat flux. Further engineering of anisotropy could be achieved by rotation of the composite with respect to applied temperature gradient inducing off-diagonal terms in thermal conductivity tensor.

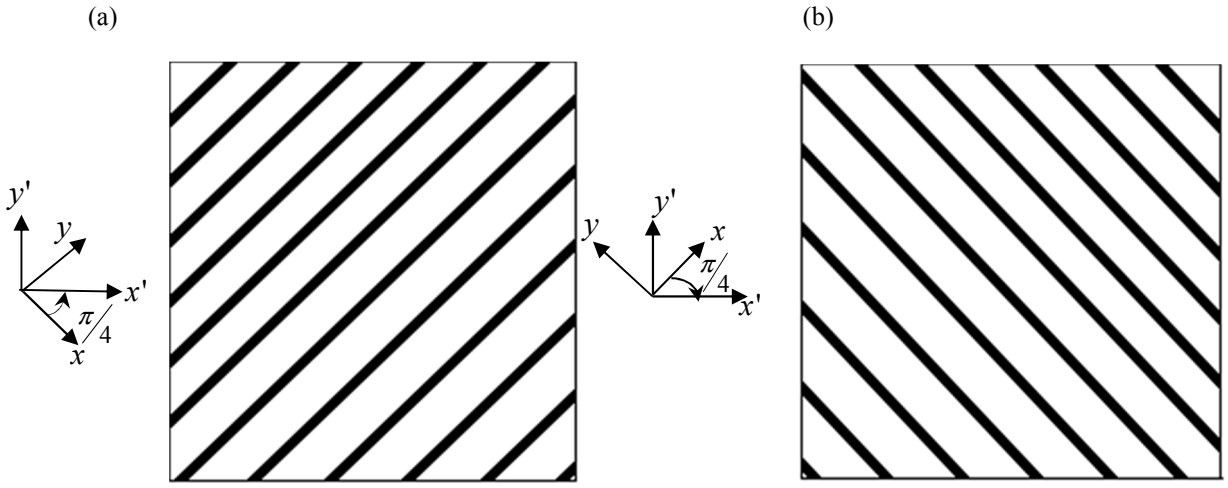

Figure A1.2: Showing the rotation of composite by (a) θ=45° and (b) θ=–45°.

The modified thermal conductivity is then;

$$\kappa_{ij}^{\ \theta} = \frac{J\kappa_{ij}J^T}{\det(J)} \tag{A1.2}$$

J is the Jacobian matrix of the coordinate transformation between the original *vs.* modified coordinate systems, J^T is the transpose of the J, and $\det(J)$ is the determinant of J.

$$\kappa_{ij}^{\ \theta} = \begin{pmatrix} \kappa_x \cos^2\theta + \kappa_y \sin^2\theta & (-\kappa_x + \kappa_y)\cos\theta\sin\theta & 0 \\ (-\kappa_x + \kappa_y)\cos\theta\sin\theta & \kappa_x \sin^2\theta + \kappa_y \cos^2\theta & 0 \\ 0 & 0 & \kappa_z \end{pmatrix} = \begin{pmatrix} \kappa_{xx}^{\ \theta} & \kappa_{xy}^{\ \theta} & 0 \\ \kappa_{yx}^{\ \theta} & \kappa_{yy}^{\ \theta} & 0 \\ 0 & 0 & \kappa_z \end{pmatrix}. \tag{A1.3}$$

The modified Fourier law;

$$q_i^{\ \theta} = -\kappa_{ij}^{\ \theta} \nabla T_j^{\ \theta}.$$

$$\begin{pmatrix} q_x{}^{\theta} \\ q_y{}^{\theta} \\ q_z{}^{\theta} \end{pmatrix} = -\begin{pmatrix} \kappa_{xx}{}^{\theta} & \kappa_{xy}{}^{\theta} & 0 \\ \kappa_{yx}{}^{\theta} & \kappa_{yy}{}^{\theta} & 0 \\ 0 & 0 & \kappa_z \end{pmatrix} \begin{pmatrix} \partial T/\partial x' \\ \partial T/\partial y' \\ \partial T/\partial z' \end{pmatrix}. \tag{A1.4}$$

Applying constant temperature gradient (∇T_x) along the x';

$$\begin{aligned} q_x{}^{\theta} &= -\kappa_{xx}{}^{\theta} \nabla T_{x'} \\ q_y{}^{\theta} &= -\kappa_{yx}{}^{\theta} \nabla T_{x'} \end{aligned}. \tag{A1.5}$$

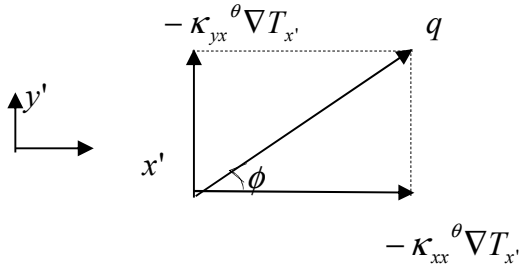

Figure A1.3: The heat flux density vectors in *x'* and *y*' directions.

The heat flux bending angle (ϕ) in a rotated composite is;

$$\phi = \tan^{-1}\left(\frac{q_y}{q_x}\right) = \tan^{-1}\left(\frac{\kappa_{yx}{}^{\theta}}{\kappa_{xx}{}^{\theta}}\right) = \tan^{-1}\left(\frac{(-\kappa_x + \kappa_y)\cos\theta\sin\theta}{\kappa_x \cos^2\theta + \kappa_y \sin^2\theta}\right)$$

$$= \tan^{-1}\left(\frac{\left(-(l_1+l_i)^2\left(\frac{\kappa_1}{\kappa_i}\right) + \left(\frac{\kappa_1}{\kappa_i}\right)l_1^2 + \left(\frac{\kappa_1}{\kappa_i}\right)^2 l_1 l_i + l_1 l_i + \left(\frac{\kappa_1}{\kappa_i}\right)l_i^2\right)\cos\theta\sin\theta}{(l_1+l_i)^2\left(\frac{\kappa_1}{\kappa_i}\right)\cos^2\theta + \left(\left(\frac{\kappa_1}{\kappa_i}\right)l_1^2 + \left(\frac{\kappa_1}{\kappa_i}\right)^2 l_1 l_i + l_1 l_i + \left(\frac{\kappa_1}{\kappa_i}\right)l_i^2\right)\sin^2\theta}\right) \tag{A1.6}$$

Where $a = (l_1+l_i)^2\left(\frac{\kappa_1}{\kappa_i}\right)$ and $b = \left(\frac{\kappa_1}{\kappa_i}\right)l_1^2 + \left(\frac{\kappa_1}{\kappa_i}\right)^2 l_1 l_i + l_1 l_i + \left(\frac{\kappa_1}{\kappa_i}\right)l_i^2$

$$\phi = \tan^{-1}\left(\frac{(-a+b)\cos\theta\sin\theta}{a\cos^2\theta + b\sin^2\theta}\right) \tag{A1.7}$$

The ϕ is a function of composite layer rotation angle θ, thermal conductivity ratio of the isotropic material and interface κ_1/κ_i , thicknesses of the isotropic material l_1 and interface l_i.

A2. Computing the temperature derivatives

The first order derivatives were computed as follows:

$$\left.\frac{\partial T}{\partial x}\right|_{(x,y)} = \frac{T(x+5\Delta x,y)-T(x,y)}{5\Delta x} \qquad \left.\frac{\partial T}{\partial y}\right|_{(x,y)} = \frac{T(x,y+5\Delta y)-T(x,y)}{5\Delta y} \tag{A2.1}$$

Here, $T(x,y)$ corresponds to a point in the matrix (130 X 130) of temperature readings. The temperature difference, in the numerator corresponds to the difference between five IR camera recorded spot sizes, incorporating the interface. ($l_{Al} = 1.7$ mm, $5x0.385 = 1.925$ mm)

The second order derivatives were computed, through a forward difference method, as follows:

$$\left.\frac{\partial^2 T}{\partial x^2}\right|_{(x,y)} = \frac{\left.\frac{\partial T}{\partial x}\right|_{(x+5\Delta x,y)} - \left.\frac{\partial T}{\partial x}\right|_{(x,y)}}{5\Delta x} = \frac{T(x+10\Delta x,y)+T(x,y)-2T(x+5\Delta x,y)}{(5\Delta x)^2}$$

$$\left.\frac{\partial^2 T}{\partial y^2}\right|_{(x,y)} = \frac{\left.\frac{\partial T}{\partial y}\right|_{(x,y+5\Delta y)} - \left.\frac{\partial T}{\partial y}\right|_{(x,y)}}{5\Delta y} = \frac{T(x,y+10\Delta y)+T(x,y)-2T(x,y+5\Delta y)}{(5\Delta y)^2}$$

$$\left.\frac{\partial^2 T}{\partial x\,\partial y}\right|_{(x,y)} = \frac{\left.\frac{\partial T}{\partial x}\right|_{(x,y+5\Delta y)} - \left.\frac{\partial T}{\partial x}\right|_{(x,y)}}{5\Delta y} = \tag{A2.2}$$

$$= \frac{T(x+5\Delta x,y+5\Delta y)-T(x+5\Delta x,y)-T(x,y+5\Delta y)+T(x,y)}{(5\Delta y)(5\Delta x)}$$

1.6 References

[1] M. Kadic, T. Bueckmann, R. Schittny, and M. Wegener, Reports Prog. Phys. **76**, (2013).

[2] D.R. Smith, J.B. Pendry, and W. M., Science **305**, 788 (2004).

[3] J.B. Pendry, A.J. Holden, D.J. Robbins, and W.J. Stewart, IEEE Trans. Microw. Theory Tech. **47**, 2075 (1999).

[4] A.A. Joshi and A. Majumdar, J. Appl. Phys. **74**, 31 (1993).

[5] K.P. Vemuri and P.R. Bandaru, Appl. Phys. Lett. **103**, 133111 (2013).

[6] M.P. Harmer, Science **332**, 182 (2011).

[7] B.-W. Kim, S.-H. Park, R.S. Kapadia, and P.R. Bandaru, Appl. Phys. Lett. **102**, 243105 (2013).

[8] D.G. Cahill, W.K. Ford, K.E. Goodson, G.D. Mahan, A. Majumdar, H.J. Maris, R. Merlin, and S.R. Phillpot, J. Appl. Phys. **93**, 793 (2003).

[9] E.T. Swartz and R.O. Pohl, Rev. Mod. Phys. **61**, 605 (1989).

[10] R.S. Prasher, Proc. IEEE **94**, 1571 (2006).

[11] S. Narayana and Y. Sato, Phys. Rev. Lett. **108**, 214303 (2012).

[12] T. Yang, K.P. Vemuri, and P.R. Bandaru, Appl. Phys. Lett. **105**, 083908 (2014).

[13] C.-W. Nan, R. Birringer, D.R. Clarke, and H. Gleiter, J. Appl. Phys. **81**, 6692 (1997).

[14] S.T. Huxtable, D.G. Cahill, S. Shenogin, L. Xue, R. Ozisik, P. Barone, M. Usrey, M.S. Strano, G. Siddons, M. Shim, and P. Keblinski, Nat. Mater. **2**, 731 (2003).

CHAPTER 2: ENHANCED SOLAR EVAPORATION OF WATER FROM POROUS MEDIA, THROUGH CAPILLARY MEDIATED FORCES AND SURFACE TREATMENT

2.1 Introduction

The enhancement of the efficiency of evaporation of liquid water, for water evaporation and steam generation, is of major technological as well as scientific interest, with applications ranging from water heaters to distillation and desalination [1]. The use of solar radiation for this purpose amounts to a better utilization of an abundant energy resource [2,3]. While evaporation from planar surfaces is typically due to the differences between (a) the saturation vapor pressure and the internal liquid pressure, as well as (b) the temperature difference between the surface and the ambient, the use of porous media and heat localization may provide an alternate path, as has recently been proposed [4]. Such a scheme involves coupling the absorbed heat with capillary flow in porous media, where the "wicking" of the liquid in the channels provides a driving force for the liquid flow and subsequent evaporation. Much related work has focused on the chemical aspects of the process,[5] as related to or enhanced light capture, e.g., through the use of plasmonic characteristics [6,7] of nanoparticles [8-10]/-shells [6,11,12]. However, considering that the efficacy of nanoparticles in enhancing convective heat transfer is debated [13], it would also be pertinent to consider the underlying mechanical and surface forces that may dictate the evaporation efficiency. It is then the aim of this chapter to probe such fundamental aspects, related to the role of thermal and fluid transport [14], coupled with materials characteristics.

2.2 Experimental

The experiments: Fig. 2.1(a), related to probing such characteristics were carried out using carbon foam (from Reynolds Inc.) based porous media, with varying pore sizes

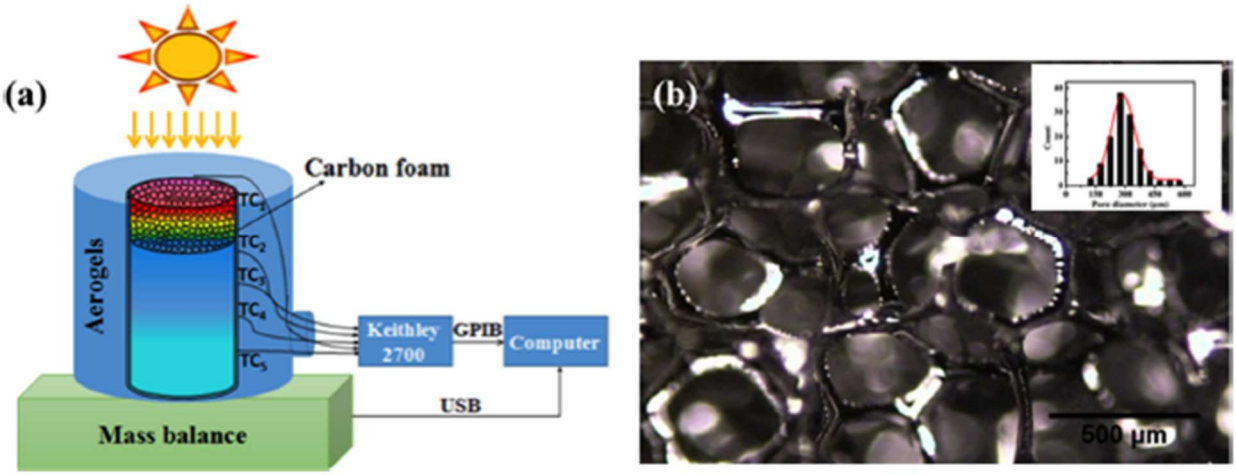

Figure 2.1: (a) Experimental setup, related to solar radiation mediated evaporation of water. A solar light simulator was used as an input power source for heating the water in the porous carbon foams, insulated laterally through a low thermal conductivity, aerogel infiltrated, chamber. The thermocouples (TC) probe the water and vapor temperature along the height of the beaker, while the mass balance at the bottom was calibrated for the mass loss (Δm) due to water evaporation. (b) A SEM (scanning electron microscope) micrograph of the top surface of a typical porous structure of the carbon foams used in the experiments. The inset indicates a pore size variation distribution for a 80 PPI sample (with a mean pore size of 288 μm and a standard deviation of ~59 μm).

(characterized in terms of pores per inch: PPI), albeit at a fixed porosity of 97%. We report on the results of particular samples with 45 PPI (with an average pore diameter, d ~ 546 μm), 60 PPI (d ~ 422 μm), 80 PPI (d ~ 288 μm), and 100 PPI (d ~ 253 μm) with a typical distribution (see Appendix, Section A1) of the pore sizes: Fig. 2.1(b) and inset. While the temperatures along the height of the aerogel insulated container – ranging from below the foam to above the foam (sampling the water vapor temperature) were monitored through appropriately placed thermocouples (TC), the evaporative heat flux was parameterized in terms of a mass loss/change (Δm) of the water from the beaker, which was measured through a well-calibrated mass balance. All the possible heat losses due to convective and radiative effects were carefully considered and calibrated.

2.3 Results and Discussion

It was apparent from the results: Fig. 2.2(a) that Δm was approximately linear with waiting time (t) and more pronounced at smaller pore sizes/average pore diameter (d). The rate of the mass loss (=d(Δm)/dt): Fig. 2.2(b), obtained through the derivatives of the curves in Fig. 2.2(a), indicates that a steady state was reached at longer times, with a larger change for smaller d. The steady state may be related to equilibrium between evaporation and the reverse process of

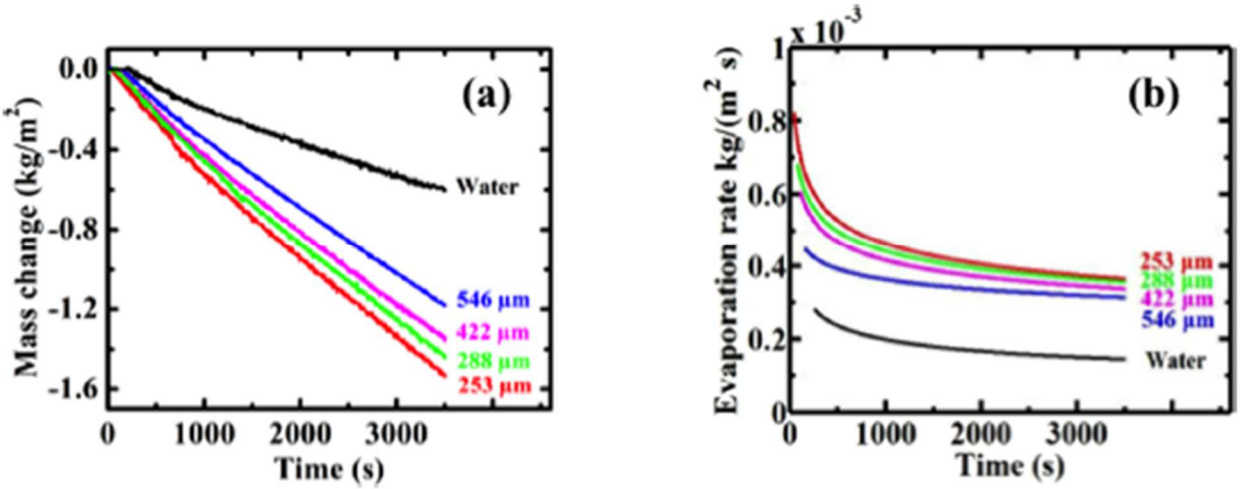

Figure 2.2: (a) The variation of the area averaged evaporative mass flux loss (Δm) with time (t) indicates the greater effectiveness of smaller pore sizes, compared to bare water. (b) The derived rate of the mass loss (=d(Δm)/dt), indicates non-uniform evaporation and that a steady state is reached at longer times, with a larger time at smaller d.

condensation, e.g., due to vapor buildup in the space above the sample. We also note that a reduced pore size resulted in a faster commencement of evaporation. In the present reported set of experiments, it was not specifically aimed to enhance the evaporative efficiency: $\eta = (\Delta mL)/tP_s$, indicating the mass loss of the liquid water transforming into vapor over a given time (t), with L as the latent heat of evaporation, and P_s the input solar radiation power. Instead, the objective was to probe a relatively simple materials platform with respect to the thermal and mechanical forces. However, we estimate an efficiency of the order of ~ 60% from the presented data, with a P_s of ~ 1700W/m^2, provided by a solar simulator.

Generally, in solar evaporation involving porous media, there are several variables that govern the efficiency via the throughput and conversion of the liquid water, to water vapor. These include, e.g., (a) the constitution and characteristics of the materials in the porous medium and related chemistry [15], (b) the pore size and the distribution, (c) the relative contribution of conductive and convective heat transfer, etc. The net outwards mass flux (Δm) across the interface (considering the difference of the evaporation and the condensation) has generally been considered to be a function of several intensive variables [16], in addition to the specific characteristics of the liquid (e.g., the density: ρ_l, thermal conductivity: κ_l, dynamic viscosity: μ, the surface tension: σ, the latent heat of evaporation: L) at/close to the interface such as the equilibrium vapor pressure (/temperature) at the liquid (l)/vapor (v) interface: $P_{lv}(/T_{lv})$. At the interface of the liquid with the wall, the evaporation process was predominantly posited [16] to occur in an intermediate evaporating thin film region – between the intrinsic meniscus (i.e., corresponding to the bulk) and a non-evaporating film - also see Fig. 2.4(b). The latter region has a thickness (δ) of the order of ~ 10 nm, originates from the van der Waals forces between the solid surface and the adherent liquid, and creates a disjoining pressure: P_d ($\sim A/\delta^3$, with A as the dispersion/Hamaker constant) [17]. The P_d may be a major influence for polar liquids such as liquid water and result in a modulation of the evaporative characteristics. It should also be noted that the thin film thickness profiles have been previously considered to be invariant beyond a critical channel radius of the order of ~ 2.5 μm [18].

Most importantly, the influence of the capillary pressure (P_c) in the liquid flow through the porous media, as well as in modifying the thin film curvature should also be considered. The P_c is related to the σ as well as the interfacial curvature ($K = y''(z)(1 + y'(z)^2)^{-3/2}$), through $P_c = \sigma K$, where $y''(z)$ and $y'(z)$ are the second and first derivatives of the thickness of the film with

respect to the height (z) along the pore. Considering a very simple model of flow through a circular pipe in response to a capillary pressure difference ($Pc \sim \Delta P \sim 4\sigma/d$) along the height of the pore channel, the flow rate (m^3/s): $Q = (\pi d^4)/(128\mu)\ \Delta P/H$. For a d = 253 μm, and $\Delta P \sim 1.15$ kPa, the Q was estimated to be $\sim 10^{-8}$ m^3/s or equivalently $\sim 10^{-5}$ kg/s for water. From Q as the product of the cross sectional area (=A) and the flow velocity ($= v_s$), we estimate a v_s of ~ 0.2 m/s. While a greater P_c (e.g., due to a reduced d) would be expected to reduce the evaporative driving force due to increased liquid flow, it may also result in a flatter liquid profile in the evaporating thin film. Consequently, the thermal gradient could be reduced with the possibility of increased heat transfer. The influence of the Capillary number ($Ca = \mu v_s/\sigma$, which considers the relative effects of laminar flow (say, at a velocity v_s) vs. capillary flow is pertinent. Considering Poiseuille flow-like dynamics for water (with $\mu \sim 10^{-3}$ Pa.s and $\sigma \sim 72 \times 10^{-3}$ N/m), we estimate a Ca of the order of 10^{-3}, for an ~250 μm pore diameter. Assuming heat dominated flow, where $v_s = h\Delta T/ \rho_l L$, with h as the evaporative heat transfer coefficient of the heated water, and ΔT as the superheat [19] would yield an even smaller Ca, again indicating the dominance of capillary flow.

It is also relevant to note that due to the (i) variation with temperature along the pore, and (ii) relatively small depth (related to the thickness of the carbon foam) over which water flow occurs, that the surface tension driven convection (Marangoni effect) may also need to be considered. Marangoni convection could arise in the pores due to a temperature variation in the surface tension. For instance, a smaller difference of the temperatures, e.g., between the thermocouple: TC1, and TC2 - see Fig. 2.1(a) was observed for the case of pure water (difference of ~ 2 ^oC) in contrast to the sample with 253 μm pore size (difference of ~ 15 ^oC). The pressure due to Marangoni flows, over a pore height of H (~ 1.2 cm) may be estimated

through considering the temperature variation of the surface tension ($d\sigma/dT \sim -2 \cdot 10^{-4}$N/mK, for water) as well as the thermal expansion coefficient [20] ($\alpha = 1/l \cdot dl/dT$, ~ 228 · 10^{-6}/K at 22 ºC, and ~ 437 · 10^{-6}/K at 47 ºC for water, through:

$$\frac{d\sigma}{dl}\left(= \frac{d\sigma}{dT}\frac{dT}{dl}\frac{l}{l}\right) = \frac{d\sigma}{dT}\frac{1}{\alpha}\frac{1}{l} \tag{2.1}$$

Consequently, a pressure variation from the bottom (at ~ 90 Pa) to the top of the sample (at ~ 40 Pa) drives the flows. However, the considered values of the Marangoni flow related pressure are at most 10% of the P_c contributions.

Now considering the Δm over a period of 1 hour of ~ 1.5 kg/m^2 for d = 253 μm: Fig. 2.2(a), the equivalent evaporation rate over the carbon foam (covering the beaker of diameter ~ 3.6 cm) is of the order of 4.2 · 10^{-7} kg/s – a factor of 25 lower than the value estimated through Poiseuille flow dynamics. Such a discrepancy may be ascribed to the tortuosity of the porous structure within the carbon foam. We note, for instance, that the ratio of the P_c (equivalent to $\Delta P \sim 4\sigma/d$) for the smallest average pore diameter of d = 253 μm to the largest pore diameter of d = 546 μm, in our study, is a factor of √3 higher compared to the respectively experimentally observed respective Δm ratio (i.e., 1.53 kg/m^2 for d ~ 253 μm vs. 1.21 kg/m^2 for d ~ 546 μm). As the diffusion length is proportional to the square root of the dimensionality, such a relation seems to indicate the importance of further considering the influence of pore ordering in evaporative processes. Moreover, more sophisticated mechanisms of heat transfer, e.g., where vapor is emitted while water is simultaneously drawn into the internal cavities/tunnels [21] may be relevant but are difficult to apply in our present case due to the lack of precise knowledge of pore structure.

We then conclude that relatively minor contributions to evaporation arise from (a) the evaporative thin film region [16], e.g., incorporating the triple-line region [22], and (b) thermocapillary convection due to Marangoni flows. Instead, capillary induced Poiseuille flows [23] seem to provide a rationale for the observed experimental results. Consequently, the efficiency of the water evaporation may be parameterized through the Ca, with a lower Ca being beneficial. Indeed, such a conclusion was previously drawn [24] in a study on the drying of porous media, through considering the formation and flow of macroscopic liquid films on the porous surface. However, even/uniform evaporation must be balanced with the lower throughput of the water vapor/steam generation.

The experimentally observed variation of the temperature along the height of the beaker indicates a progressive heating, which saturates as a function of time. Such behavior was analyzed as due to the competing effects of conduction and convection. From energy balance, a resultant evaporative heat flux from an effective surface area of As due to the instantaneous temperature difference between the water in the carbon foam: at a temperature T(t), and the ambient: at a temperature Ta, yields a convective heat flux (= $hA_s[T(t) - T_a]$). Such a flux is assumed to be due to the water mass loss (=$d(\Delta m)/dt = \rho VCdT(t)/dt$), where ρ is the water density, V is the volume, and C the specific heat of the water in the porous medium. Consequently, it may be derived, for an initial water temperature: T_i, that:

$$\frac{T(t)-T_a}{T_i-T_a} = exp\left(-\frac{hA_s}{\rho VC}t\right) \tag{2.2}$$

Plots of the TC1 temperature: T(t) fit to the above relation are shown in Fig. 2.3(a), comparing a bare water surface and the studied porous surfaces (see Appendix, Section A2). We noted that the plots in Fig. 2.3(a), could be distinguished through the increased hA_s/ VC ratio as a function of the pore size. For instance, in the case of pure water, we obtained a value for the ratio

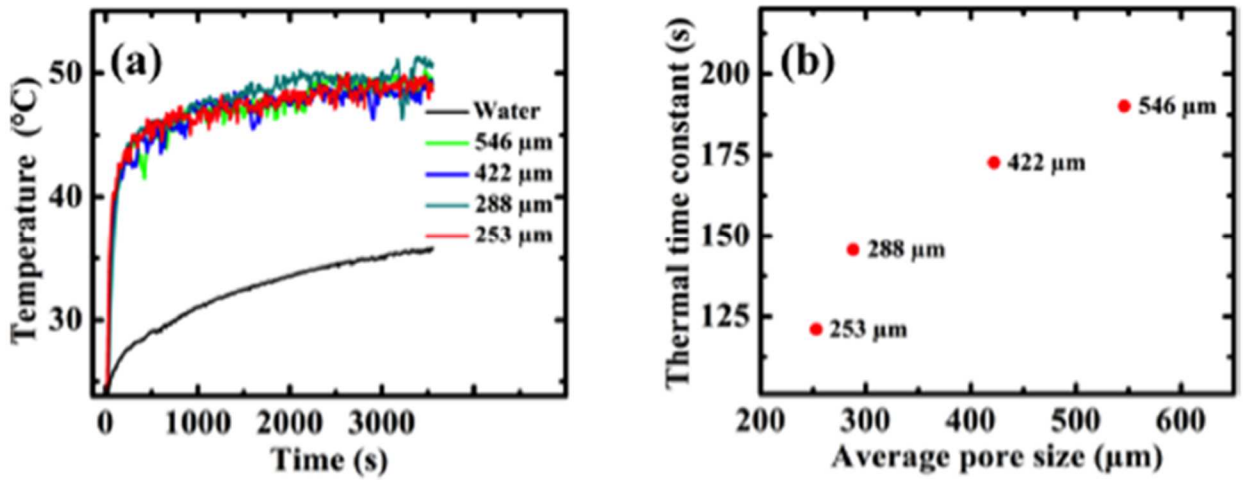

Figure 2.3: (a) The observed variation of the TC1 temperature from a bare water surface compared to that in the studied porous surfaces indicates competing effects of conductive and convective heat transfer, (b) A plot of the deduced thermal time constant, for water evaporation, as a function of the pore size.

of ~ 9.3 x 10−4, yielding a value of h ~ 47 W/m^{2}K, while for the smallest d ~ 253 µm, the corresponding ratio is ~ 8.3 x 10−3, yielding a value of h enhanced almost by an order of magnitude to ~ 420 W/m^{2}K. The inverse of the ratio is commonly considered in terms of a thermal time constant (i.e., $\tau = \rho VC/hA_s$), as treated through a lumped element approach [20], with $1/hA_s$ indicating a resistance to convective heat transfer and ρVC being the capacitance of the water in the porous medium, and is plotted in Fig. 2.3(b). Given that the porosity of all the studied carbon foams is ~ 97%, we may interpret the varying time constants as due to the increase of the h with reduced pore size. Indeed, the possibility of rough enhanced surfaces for increased heat transfer has been considered in much detail [25,26].

In addition to the influence of pore size on regulating the rate of water evaporation through convective methodologies, we attempted to investigate the role of the materials surface. The related specific characteristics have been focused on the P_d but may play a larger role. For example, it may be thought that increased hydro-/phobicity (/- philicity) would retract (/advance) the evaporative thin film region over which evaporation effectively occurs. Consequently, it was hypothesized that inducing hydrophilic character onto the carbon foam surface would effectively

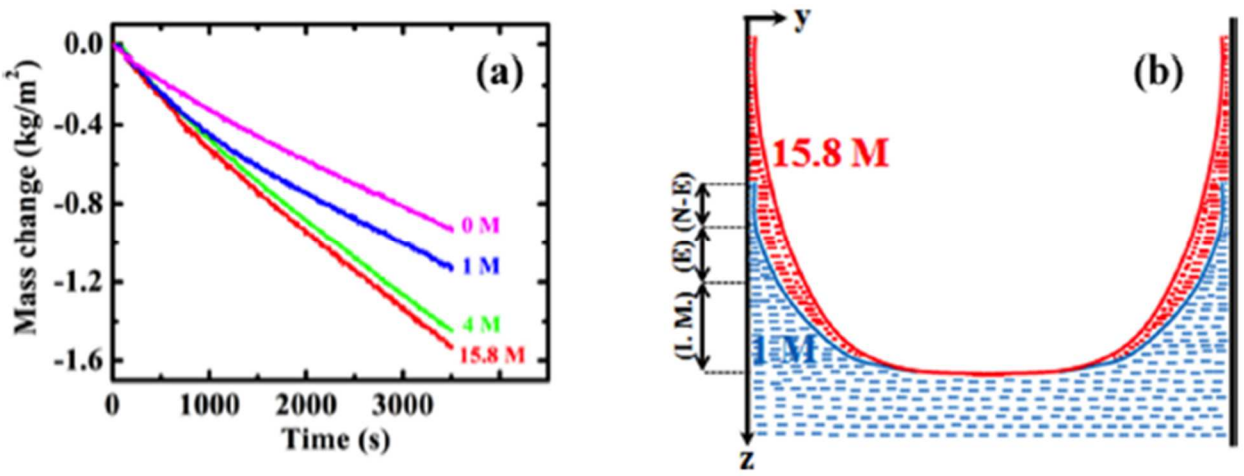

Figure 2.4: (a) The variation of the evaporative mass flux loss (Δm) with time as a function of increased molarity of nitric acid, which was used to enhance the hydrophilic character of the carbon foam surface. (b) The inferred variation in the meniscus shape indicating an increased evaporative thin film region, due to enhanced surface hydrophilicity through larger nitric acid molarity (15.8 M vs. 1 M) treatment of the carbon foam surface The I.M. (Intrinsic meniscus), E. (evaporating thin film) and N-E (non-evaporating region) regions are shown.

flatten the film profile [18], over the meniscus region, due to creep of the water up the sides of the pores, and enhance the P_c. To this end, the carbon foams used for the porous media were subject to nitric acid (HNO3) treatment for two hours, under sonication, which has been shown previously to oxidize the graphitic surface and introduce hydrophilic functional group [27]. An increasing molarity of the acid was used to enhance hydrophilic character. It was then observed that the Δm was increased, with a reduced waiting time observed at any given pore size, with increased molarity: Fig. 2.4(a) indicates the data for d = 253 μm; – also see Appendix, Section A3). An increased effective hydrophilic interaction seems to be implied, contributing to enhanced evaporation akin to effects related to a reduced pore size, cf., Fig. 2.2(a). We depict the inferred variation in the meniscus shape indicating an increased evaporative thin film region at increased surface hydrophilicity of the carbon foam surface in Fig. 2.4(b), which in turn leads to enhanced evaporative mass flux.

2.4 Conclusion

In summary, we have shown that enhanced capillary pressures, either due to a decreased pore size or the chemical modification of the surfaces would serve to increase the evaporative efficiency of water through light absorbing (see Appendix, section A4), where it is indicated that the absorption could be of the order of 93%-95%) porous media. The proposed media may also be used for desalination (see Appendix, section A5) where the larger σ may be of advantage; additionally, a decreased interfacial thermal resistance [28] in ionic solutions may also be beneficial.

Chapter 2, in full, has been published in "Enhanced solar evaporation of water from porous media, through capillary mediated forces and surface treatment", AIP Advances 6, 085218 (2016) by M. Fatih Canbazoglu, B. Fan, A. Kargar, K. Vemuri, and P.R. Bandaru. The dissertation author was the primary researcher and author of this material.

2.5 Appendix

A1. Pore Analysis:

45 PPI :

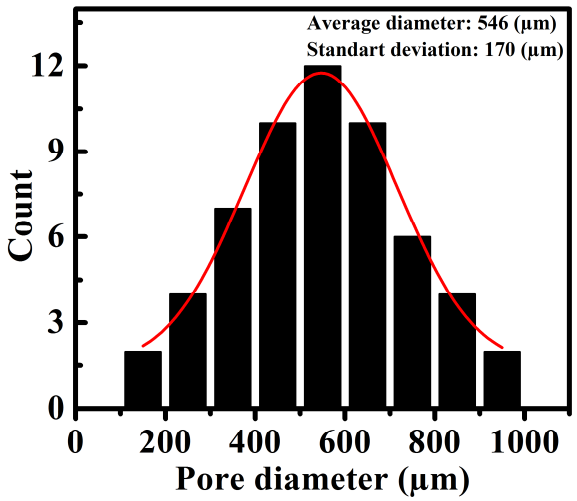

60 PPI :

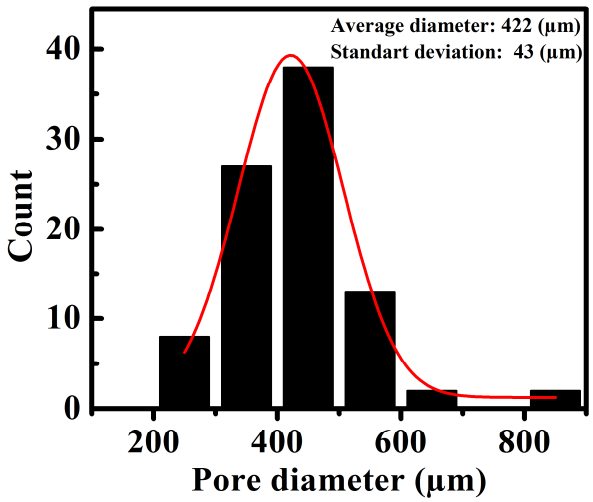

80 PPI :

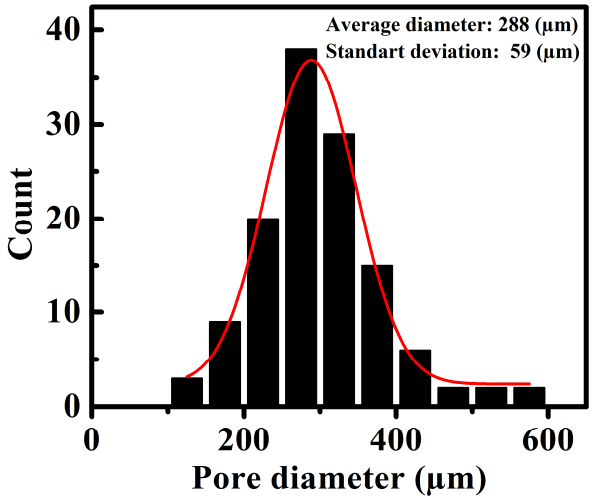

100 PPI :

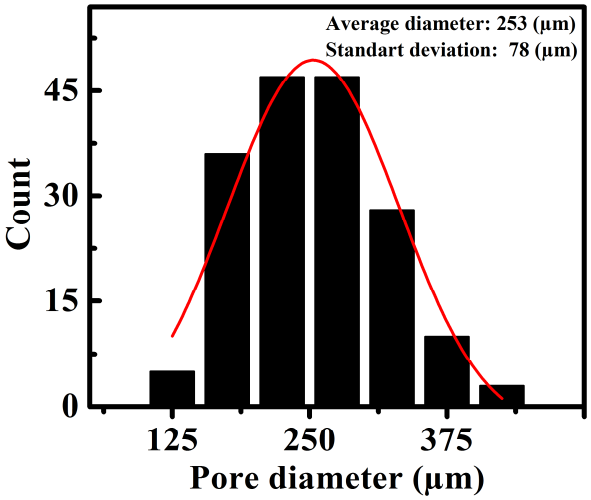

A2. Temperature profile results:

Water case (No-foam):

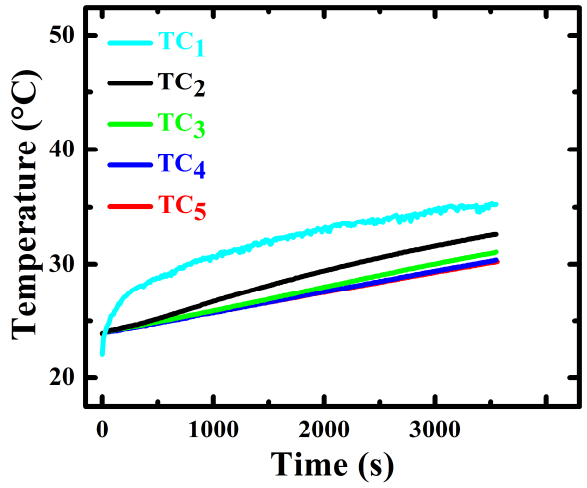

Carbon foam (253 μm):

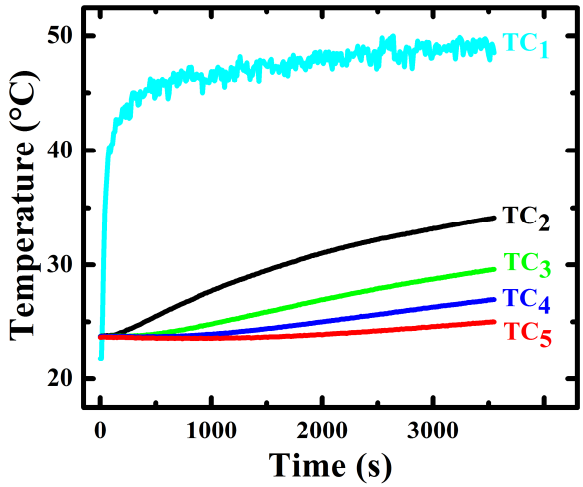

A3. Hydrophobic/philic effect on solar steam generation:

Carbon foam (546 μm):

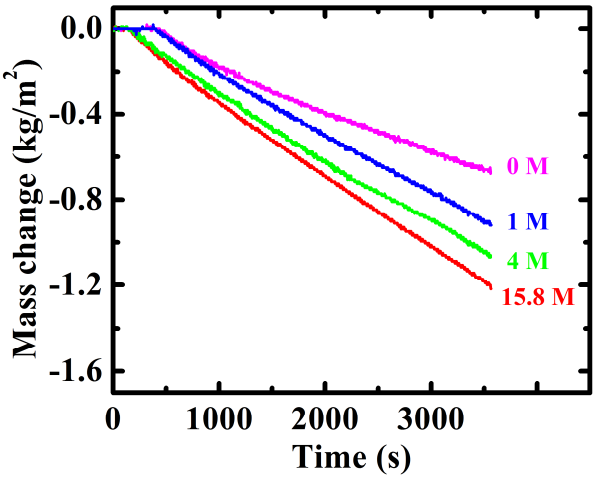

Carbon foam (422 μm):

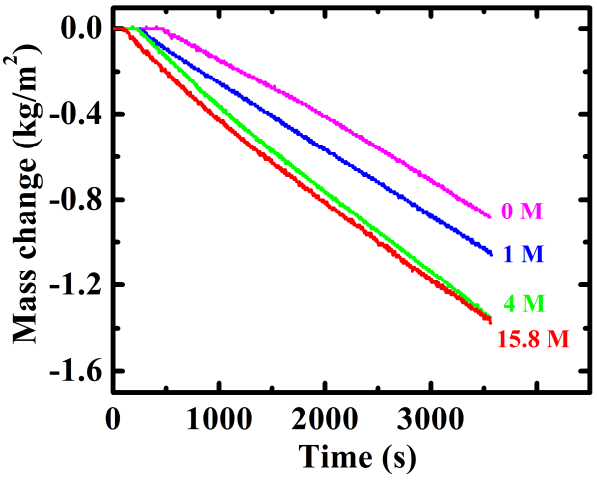

Carbon foam (288 μm):

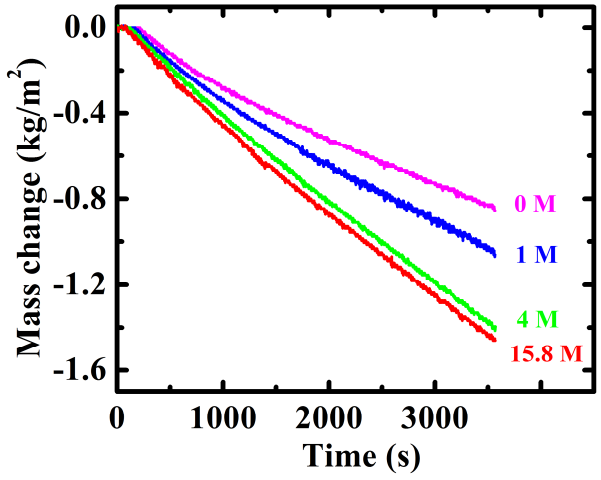

Carbon foam (253 μm):

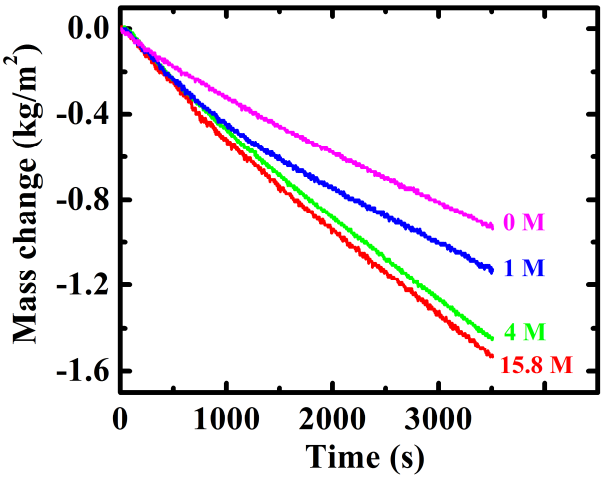

A4. Optical properties of carbon foam:

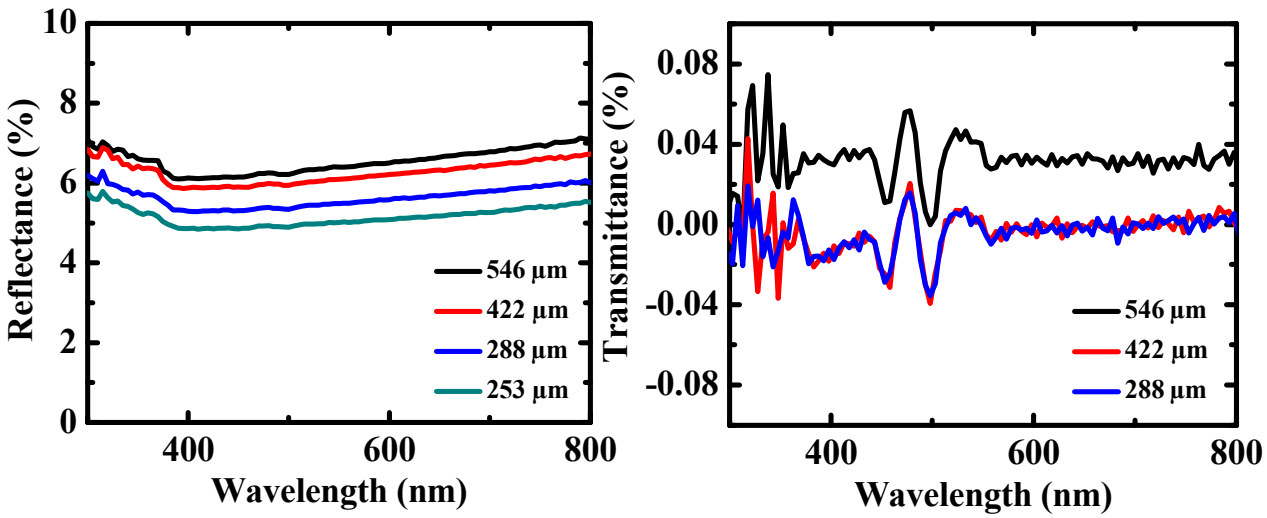

Reflectance and transmittance measurements were obtained using a 150 mm integrating sphere connected to a LAMBDA 1050 UV/Vis/NIR spectrophotometer.

A5. Desalination performance of the system:

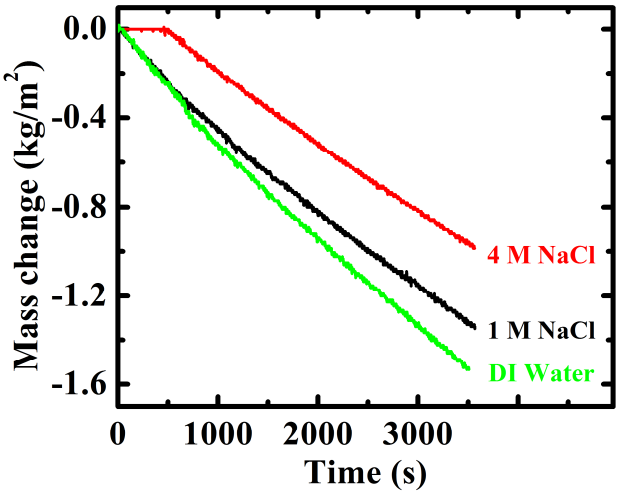

2.6 References

[1] K. Sampathkumar, T. V. Arjunan, P. Pitchandi, and P. Senthilkumar, Renew. Sustain. Energy Rev. **14**, 1503 (2010).

[2] M. Thirugnanasambandam, S. Iniyan, and R. Goic, Renew. Sustain. Energy Rev. **14**, 312 (2010).

[3] N. S. Lewis, Science **80**, 6271 (2016).

[4] H. Ghasemi, G. Ni, A. M. Marconnet, J. Loomis, S. Yerci, N. Miljkovic, and G. Chen, Nat. Commun **5**, 4449 (2014).

[5] L. Zhang, B. Tang, J. Wu, R. Li, and P. Wang, Adv. Mater. **27**, 4889 (2015).

[6] K. Bae, G. Kang, S. K. Cho, W. Park, K. Kim, and W. J. Padilla, Nat. Commun. **6**, 10103 (2015).

[7] L. Zhou, Y. Tan, D. Ji, B. Zhu, P. Zhang, J. Xu, Q. Gan, Z. Yu, and J. Zhu, Sci. Adv. **2**, 1501227 (2016)

[8] S. Ishii, R. P. Sugavaneshwar, and T. Nagao, J. Phys. Chem. C. **120**, 2343 (2016).

[9] S. Ishii, R. P. Sugavaneshwar, K. Chen, T. D. Dao, and T. Nagao, Opt. Mater. Express **6**, 640 (2016).

[10] X. Wang, G. Ou, N. Wang, and H. Wu, ACS Appl. Mater. Interfaces **8**, 9194 (2016).

[11] M. S. Zielinski, J.-W. Choi, T. La Grange, M. Modestino, S. M. H. Hashemi, Y. Pu, S. Birkhold, J. A. Hubbell, and D. Psaltis, Nano Lett. **16**, 2159 (2016).

[12] O. Neumann, A. D. Neumann, E. Silva, C. Ayala-Orozco, S. Tian, P. Nordlander, and N. J. Halas, Nano Lett. **15**, 7880 (2015).

[13] S. Lee, R. A. Taylor, L. Dai, R. Prasher, and P. E. Phelan, Mater. Res. Express **2**, 065004 (2015).

[14] S. J. S. MORRIS, J. Fluid Mech. **494**, 297 (2003).

[15] S. Yu, Y. Zhang, H. Duan, Y. Liu, X. Quan, P. Tao, W. Shang, J. Wu, C. Song, and T. Deng, Sci. Rep. **5**, 13600 (2015).

[16] M. Potash and P. Wayner, Int. J. Heat Mass Transf. **15**, 1851 (1972).

[17] J. N. Israelachvili, Intermolecular and Surface Forces, 3rd ed. (Academic Press, San Diego, CA, 2011).

[18] H. Wang, S. V. Garimella, and J. Y. Murthy, Int. J. Heat Mass Transf. **50**, 3933 (2007).

[19] H. K. Cammenga, Current topics in materials science (North Holland Publishing Company, New York, NY, 1980)

[20] W. Nakayama, T. Daikoku, H. Kuwahara, and T. Nakajima, J. Heat Transfer **102**, 451 (1980).

[21] H. K. Dhavaleswarapu, J. Y. Murthy, and S. V. Garimella, Int. J. Heat Mass Transf. **55**, 915 (2012)

[22] P. K. Kundu and I. M. Cohen, Fluid Mechanics, 4th ed. (Academic Press, San Diego, CA 2008).

[23] A. G. Yiotis, A. G. Boudouvis, A. K. Stubos, I. N. Tsimpanogiannis, and Y. C. Yortsos, Phys. Rev. E. **68**, 037303 (2003).

[24] T. L. Bergman, A. S. Lavine, F. P. Incropera, and D. P. Dewitt, Introduction to Heat Transfer (John Wiley Inc. Hoboken, NJ, 2011)

[25] A. E. Bergles, J. Heat Transfer **110**, 1082 (1988).

[26] L. Burmeister, Convective Heat Transfer, 2nd ed. (John Wiley & Sons Inc., New York, NY, 1993)

[27] E. Bouleghlimat, P. R. Davies, R. J. Davies, R. Howarth, J. Kulhavy, and D. J. Morgan, Carbon N. Y. **61**, 124 (2013).

[28] S. Baral, A. J. Green, and H. H. Richardson, MRS Proc. **1779**, 33 (2015)

CHAPTER 3: ENHANCED SOLAR THERMAL EVAPORATION OF ETHANOL-WATER MIXTURES, THROUGH THE USE OF POROUS MEDIA

3.1 Introduction

The harness of solar energy could be accelerated through heat localization in porous media, which may then be used for applications ranging from enhanced evaporation of water [1,2] to distillation schemes involving desalination[3,4]. While many such schemes utilize nanoparticles, as related to their ease of heating, it should also be considered that the rate of heat loss may be large as well. Additionally, issues related to the ease of uniformly dispensing the particles, agglomeration, and sensitivity to ambient, must also be carefully considered. In this context, it may be beneficial to utilize porous carbon based media, instead. The advantages of such media include [1], *e.g.,* (i) a relatively stable and consolidated structure, (ii) tunability of pore sizes for enhanced evaporative water mass flux, (iii) possibility of meniscus engineering to increase the rate of evaporation, as well as the possibility of (iv) chemical treatment to vary the degree of hydro-philicity (-phobicity).

In this chapter, we discuss the characteristics related to the evaporation of binary liquid mixtures. While there has been significant work on the evaporation of one component liquids [5-12], there has been relatively less effort directed at understanding multicomponent systems [13]. The significance of such investigations extends to understanding fluid-fluid and fluid-surface interactions, with applications from phase separation and distillation. Specifically, we consider the ethanol (E) – water (W) mixture, which constitutes a homogeneous, positive azeotrope [14] (with a minimum boiling point at ~ 78.2 ^{o}C, at 95.6 vol% E – 4.4 vol% W mixture) compared to pure ethanol with a boiling point ($T_{bp,\,E}$ ~ 78.4 ^{o}C) and water ($T_{bp,\,W}$ ~ 100 ^{o}C). Consequently, we

sought to investigate the evaporative characteristics of mixtures less than the azeotrope composition, facilitated through the use of carbon foam (CF). The hypothesized beneficial attribute CF involves heat localization, which in turn would increase the temperature, as well as the rate of evaporation of the *E-W* mixture. The latter aspect would be manifested, *e.g.,* through an estimated convective heat transfer coefficient (h^{conv}).

3.2 Experimental

We report on the evaporative characteristics of three particular *E-W* mixtures (*i.e.,* 12.5 vol% *E,* 25 vol% *E*, and 37.5 vol% *E*) subject to an input solar radiation power (P_s) of ~ 1700 W/m^2, provided by a solar simulator, considering the mass loss (Δm) of the mixture (in units of kg/[m^2. hour]). The amount of constituent *E* in the mixtures was chosen so as to avoid abnormal

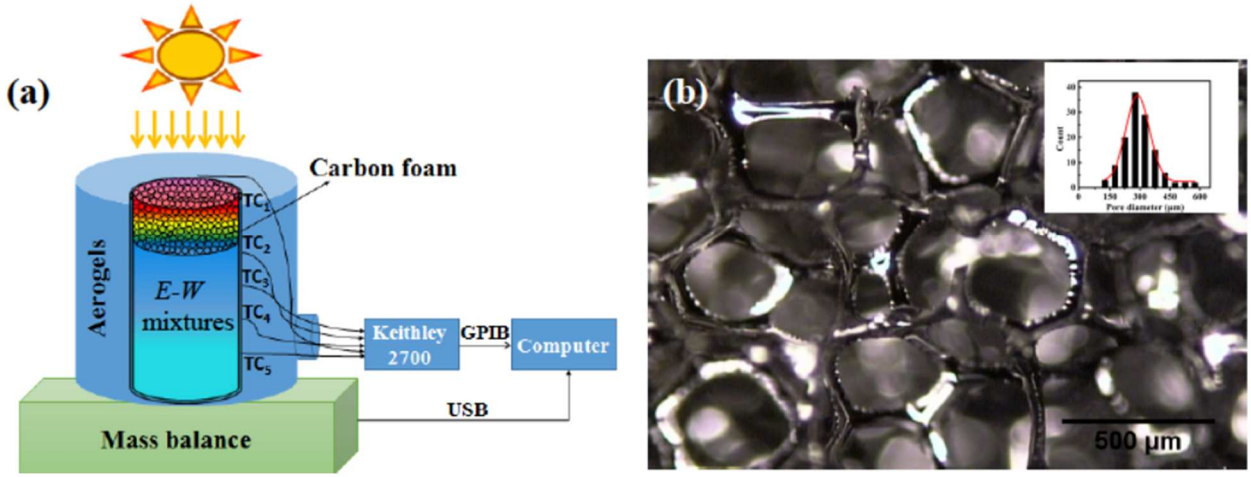

Figure 3.1: (a) Experimental setup, related to solar radiation mediated evaporation of ethanol (*E*) – water (*W*) mixtures. A solar light simulator was used as an input power source for heating the mixture in the porous carbon foams, insulated laterally through a low thermal conductivity, aerogel infiltrated, chamber. The thermocouples (TC) probe the liquid and vapor temperature along the height of the beaker, while the mass balance at the bottom was calibrated for the mass loss (Δm) due to evaporation. **(b)** A SEM (scanning electron microscope) micrograph of the top surface of a typical porous structure of the carbon foams used in the experiments. The *inset* indicates a pore size variation distribution for a 80 PPI sample (with a mean pore size of 288 µm and a standard deviation of ~ 59 µm).

evaporation behavior observed at lower *E* content [13]. We investigated both (a) bare evaporation, as well as (b) evaporation mediated by the CF. The CF was placed floating onto the *E-W* mixture, as shown in Fig. 3.1(a). We present results on a specific CF with a fixed porosity of 97% (100 pores per inch: PPI, with an average pore diameter, *d*~ 253μm): Fig. 3.1(b). Such a particular sample was chosen based on an earlier study [1], where it was found that such a constituent diameter yielded maximal evaporative efficiencies. The temperatures along the height of the beaker were monitored by appropriately placed thermocouples (TC) along with the vapor temperature (as measured by TC1) *both* with and without CF. The Δm was determined through a calibrated mass balance.

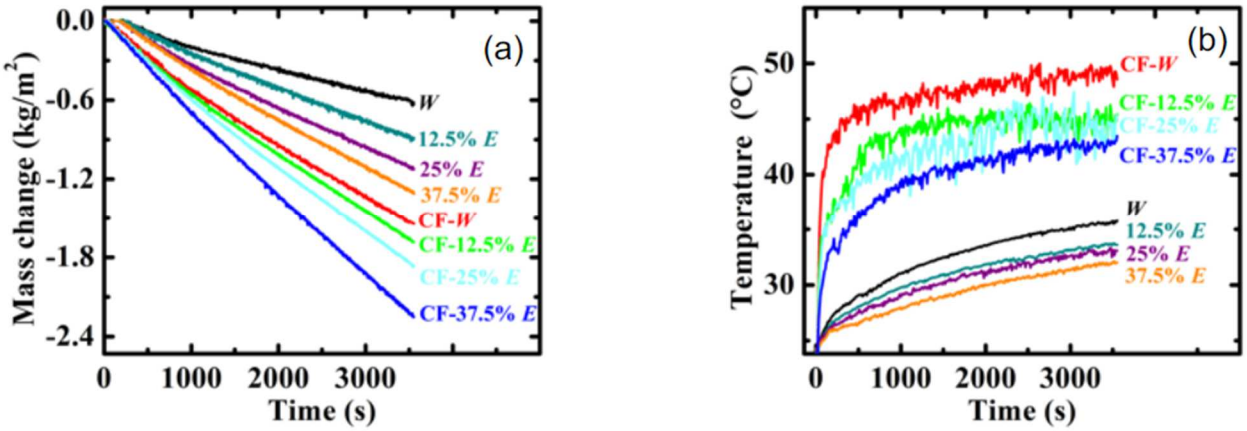

Figure 3.2: (a) The mass change/loss as a function of time of water and ethanol-water mixtures with and without carbon foam (CF), indicates a greater evaporation rate through the use of the CF. **(b**) The observed variation of the top surface temperature [TC1 – see Figure 3.1(a)] as a function of time corresponding to the mass change with and without CF.

It was apparent from the experimental results: Fig. 3.2(a), that Δm was increased by higher *E* concentration in the mixture, as well as through use of the CF. The former aspect is expected from the relatively increasing strength of the hydrogen bonding [15] - in the order of (i) *E-E,* (ii) *E-W*, and (iii) *W-W,* and related to the higher *E* volatility. The evaporation rate increases nonlinearly at a greater rate with increasing *E* concentration. A reduced initial waiting time (t_w) prior to the onset of evaporation/mass loss, along with a faster rate of temperature rise through

the use of the CF was noted: Fig. 3.2(b). It was observed that with increasing *E* content, that the ΔT (= $TC_1 - TC_5$) decreases, with temperature fluctuations presumably due to convection during evaporation. The rate of mass loss ($=d[\Delta m]/dt = \Delta m_t$) is typically a function of several variable properties [16] related to the evaporating liquid mixture, *e.g.,* the equilibrium vapor pressure (P_v), dynamic viscosity (μ), surface tension (σ), density (ρ), in concert with the related temperature (T). While P_v is a determinant of the state of evaporation, the selection of μ, σ, and ρ were done considering the related capillary pressure and the dynamics of the flow through the pores of the CF [1].

We parameterize Δm_t (P_v, μ, σ, ρ) as a function of time at various temperatures, first through dimensional analysis, *i.e.,* using the Buckingham Pi theorem [17], yielding:

$$\Delta m_t = \Delta m_t \left(P_v^{\frac{3}{2}}, \mu^2, \sigma^{-2}, \rho^{-\frac{1}{2}} \right) \tag{3.1a}$$

The mass loss/evaporation rate of the *E-W* mixture, may then be qualitatively considered to increase with the P_v as well as the μ, while being inversely related to the σ and the ρ. However, the *relative* variation in each of these, say as a function of *T* would be:

$$\frac{d(\Delta m_t)}{\Delta m_t} = Z\left(\frac{3}{2}\frac{dP_v}{P_v} + 2\frac{d\mu}{\mu} - 2\frac{d\sigma}{\sigma} - \frac{1}{2}\frac{d\rho}{\rho}\right) \tag{3.1b}$$

The Z is a constant that could be related to the extent to which the Δm_t may be well characterized by the intensive variables on the right hand side. Moreover, it is generally well known that, while the P_v increases with temperature, the μ, σ, and ρ all decrease with increasing temperature, *i.e.,* $\frac{dP_v}{P_v}$ is positive, while $\frac{d\mu}{\mu}$, $\frac{d\sigma}{\sigma}$, and $\frac{d\rho}{\rho}$ are all negative. Consequently, Eqn. (3.1b) then indicates that the evaporation rate or the volatility, with increased solar radiation exposure, is favored by the P_v, σ, and ρ while it is negatively impacted by the μ.

Considering T as the control variable we then probed the temperature variation of each of the P_v, μ, σ, and ρ, and correlated the sum variation to the experimentally determined Δm_t. At a given time (t), a correspondence was obtained to the Δm (t): Fig. 3.2(a), and t (ΔT): Fig. 3.2(b). The consequently determined P_v [$t(T)$], μ [$t(T)$], σ [$t(T)$], and ρ [$t(T)$], are indicated in Fig. 3.3.

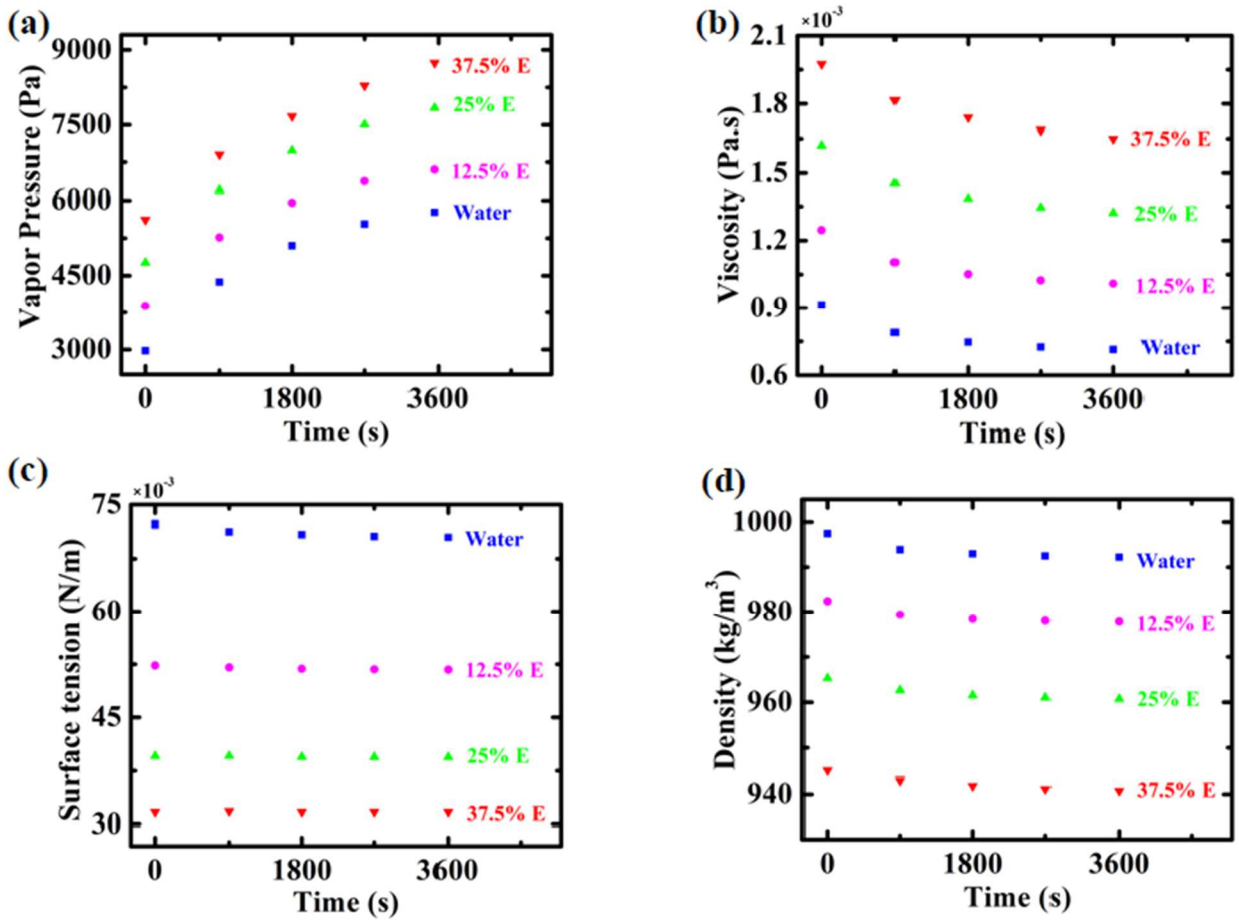

Figure 3.3: The influence of factors affecting the evaporation of ethanol-water mixtures, including **(a)** vapor pressure (Pv), **(b)** viscosity (μ), **(c)** surface tension (σ), and **(d)** density (ρ) as a function of time, with correspondence to the variation in Figure 3.2(b).

For P_v [$t(T)$] ≡ P_v (T), the vapor pressure of the E/W mixture, considering the temperature measured from TC1 – in Fig. 3.1(a), we employed the Antoine form [18]:

$$P_{v,mix}(T) = x_E \gamma_E P_E + x_W \gamma_W P_W \tag{3.2}$$

Here, the x_E and the x_W represent the mole fractions of the ethanol (E) and the water (W) in the E/W mixture, while γ_E and γ_W are the corresponding activity coefficients, and P_E and the P_W are the vapor pressures, at the given T, of the pure E and W components. The activity coefficients were evaluated from the Wilson equations [19] (see section A2. of the *Appendix*). It was assumed that the x_E and the x_W do not change in the course of the experiment on the basis that the evaporated mass is typically a small fraction (~ 1% of the total solution in the beaker). Moreover, forced convection was minimized as the experiments were all carried out in laboratory ambient. The corresponding $\mu(T)$, $\sigma(T)$ and $\rho(T)$ were estimated from the Jouyban-Acree relations [20]:

$$\ln \mu_{mix}(T) = x_W \ln \mu_w(T) + x_E \ln \mu_E(T) + 724.652\left(\frac{x_W x_E}{T}\right) + 729.357\left(\frac{x_W x_E (x_W - x_E)}{T}\right) + 976.05\left(\frac{x_W x_E (x_W - x_E)^2}{T}\right) \tag{3.3}$$

$$\ln \sigma_{mix}(T) = x_W \ln \sigma_w(T) + x_E \ln \sigma_E(T) - 488.012\left(\frac{x_W x_E}{T}\right) - 640.785\left(\frac{x_W x_E (x_W - x_E)}{T}\right) - 1073.31\left(\frac{x_W x_E (x_W - x_E)^2}{T}\right) \tag{3.4}$$

$$\ln \rho_{mix}(T) = x_W \ln \rho_w(T) + x_E \ln \rho_E(T) - 30.808\left(\frac{x_W x_E}{T}\right) - 18.274\left(\frac{x_W x_E (x_W - x_E)}{T}\right) + 13.89\left(\frac{x_W x_E (x_W - x_E)^2}{T}\right) \tag{3.5}$$

The $\frac{d(\Delta m_t)}{\Delta m_t}$ was estimated, from the experimental mass change curves – as in Fig. 3.2(a), through consideration of the change of the relevant parameters, *i.e.,* P_v, μ, σ, and ρ as a function of temperature. The discretization was done at two values of temperatures: T_1 and T_2, related to two different values of the time: t_1 and t_2, and with a temperature interval of 2 degrees K, *i.e.,* $T_2\ (t_2) = T_1(t_1) + 2$. Consequently, at two points, say 1 = (T_1, t_1) and 2 = (T_2, t_2), the variation of mass change is parameterized through:

$$\frac{d(\Delta m_t)}{\Delta m_t} = \frac{(\Delta m_t)_2 - (\Delta m_t)_1}{(\Delta m_t)_1} \tag{3.6}$$

The terms on the *right hand side* of Eqn. (3.1b), *i.e.,* the relative changes of the P_v (*i.e.,* $\frac{dP_v}{P_v}$), μ (*i.e.,* $\frac{d\mu}{\mu}$), σ (*i.e.,* $\frac{d\sigma}{\sigma}$), and ρ (*i.e.,* $\frac{d\rho}{\rho}$) were similarly evaluated at two temperature points, from the plots depicted in Fig. 3.3 – also see section A3. of the Appendix. Equating the *left* and *right* hand sides of Eqn. 3.1(b) enables the evaluation of the *Z* factor (as indicated in Table 3.1). There are two particular noteworthy aspects, related to the *Z* values, that they: (i) are close to unity (*i.e.,* in the range of 0.6-1.3), indicating the validity of the assumptions and the dimensional analysis leading to Eqn. 3.1(b), and (ii) were generally less for the CF based evaporation (*i.e.,* in the range of 0.6-0.9) compared to bare evaporative processes, presumably due to a faster rise of temperature – see Fig. 3.2(b). It was noted (see Table A3.2 in section A3 of the Appendix), that

Table 3.1: The estimated values of the *Z* of *E-W* solution mixtures, estimated per Eqn. (3.1b).

	$Z_{average}$
Water	-1.24
12.5 % E	-0.87
25 % E	-1.27
37.5 % E	-1.03
CF + Water	-0.60
CF + 12.5 % E	-0.79
CF + 25 % E	-0.88
CF + 37.5 % E	-0.69

the major positive contribution to the evaporation rate arises from the P_v change (~ 65%), while the μ accounts for ~ 30% of the rate. The combined effects of the σ and ρ are of the order of ~ 5%. The decreasing μ with increasing *T* may also be associated with a higher h^{conv} which in turn

is related to the product of the Reynolds number ($Re = v_s \rho d/\mu$) and the Prandtl number ($Pr = c_p \mu/\kappa$), where c_p is the specific heat and κ is the thermal conductivity of the mixture, *i.e.,* through $h^{conv} \sim Re^a Pr^b$, with the exponent, *a* typically [21] larger compared to *b*. Consequently, h^{conv} varies inversely with the μ. As the viscosity of the *E-W* mixture increases with *E* content, the h^{conv} decreases in spite the larger P_v of the *E* component. Generally, evaporation is typically due to the differences between the saturation vapor pressure and the internal liquid pressure, with the implication that a lower h^{conv} would be related to a higher P_v.

The experimentally observed temperature variation indicates a progressive heating of the *E-W* mixture, and leveling off with time - Fig. 3.2(b). Such behavior was analyzed as due to the competing effects of heat conduction in the porous medium coupled with convection - as related to the evaporative process. From energy balance, the resultant evaporative heat flux from an effective/evaporating surface area of A_s due to the instantaneous temperature difference between the *E-W* mixture at a temperature $T(t)$, and the ambient at a temperature T_a , yields a convective heat flux ($= h^{conv} A_s[T(t)-T_a]$). Such a flux is assumed to be due to the heat loss ($=\rho VC\, dT(t)/dt$) from the surface (both with and without the CF), with ρ and C the density and specific heat of the *E-W* mixture in the porous medium, V as the volume of the evaporating liquid (and approximately equal, in the case of the use of the CF considering the 97% porosity, to $A_s \cdot th.$, with *th.* as the thickness of the CF). Consequently, it may be derived [21], for an initial mixture temperature: T_i, that:

$$\frac{T(t)-T_a}{T_i-T_a} = exp\left(-\frac{h^{conv} A_s}{\rho VC} t\right) \tag{3.7}$$

Plots of the TC1 temperature: $T(t)$ fit to the above relation were obtained from Fig. 3.2(b), (also, see section A4. and Table A4.1 in the *Appendix*) in comparing a bare water surface

and the studied porous surfaces. For instance, in the case of pure water, we obtained a value of h^{conv} ~ 47 W/m^2·K while the use of CF yields a value of h^{conv} enhanced almost by an *order of magnitude* to ~ 420 W/ m^2·K. It was observed from an analysis of several *E-W* mixtures, that the h^{conv} (i) decreases with increasing *E* content, and is (ii) consistently larger through the use of CF for equivalent ethanol concentrations. The inverse of the ratio was considered in terms of a thermal time constant [21], (*i.e.,* $\tau = \rho VC/ h^{conv}A_s = \rho\, th.\ C/ h^{conv}$ – for the CF), with $1/ h^{conv}A_s$ indicating a resistance to convective heat transfer and ρVC being the capacitance of the *E-W* mixture in the porous medium. The larger P_v at a higher temperature yields a higher resistance to mass transfer, as seen through the larger h^{conv} value (Table 3.2). The possibility of rough enhanced surfaces for increased heat transfer has been considered previously [22,23], and is the basis for the CF porous medium.

Generally, the evaporation rate (considered in terms of Δm_t): Fig. 3.4 may be understood in terms of net heating (*both* sensible and latent) through the temperature change (ΔT): Fig. 3.2(b), and the enthalpy of evaporation (*H*), respectively. One estimate of the heating is through the thermal energy flux: $Q_{heat} = \Delta m_t C \Delta T + \Delta m_t H$, where *C* is the mass fraction averaged specific heat of the *E-W* mixture. Since *C* and ΔT are of the order of 3.5 kJ/kg·K and 20 K, while *H* is ~ 2000 kJ/kg, at the temperatures of consideration, the $\Delta m_t H$ term dominates. It was seen, both with and without the CF, that an increasing *E* content results in an increased Δm_t – from Fig. 3.4, as well as a decreased ΔT – from Fig. 3.2(b) (which yields an increased *H*). Consequently, the Q_{heat} increases with increasing *E*, and is more pronounced through the use of the CF (due to heat localization), yielding even higher evaporation rate. The heating efficiency may be estimated, through the ratio of the Q_{heat} to the solar illumination input (~1700 W/m^2) and reaches a maximum efficiency of ~ 74% for the 37.5%*E* - 62.5%*W* mixture.

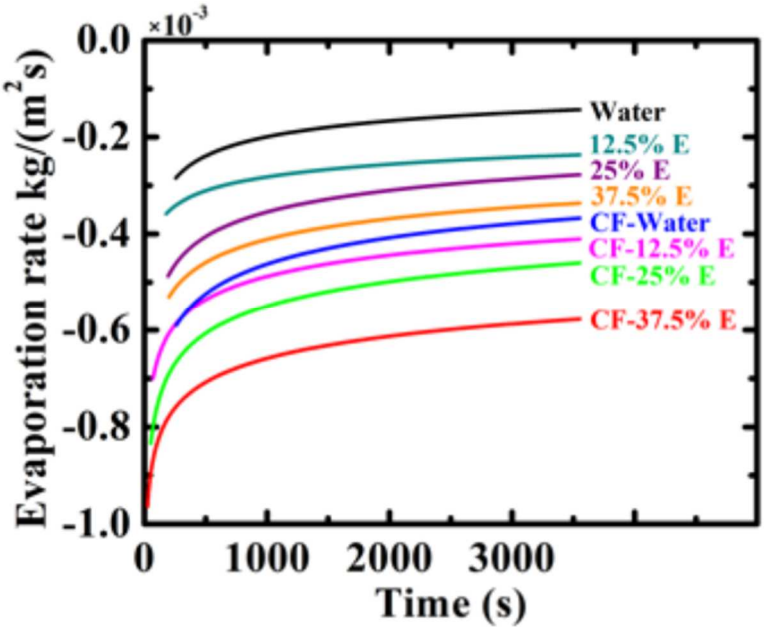

Figure 3.4: The evaporation rate (considered in terms of Δm_t) of the ethanol (E) – water (W) mixtures, is larger through the use of CF, and maybe parameterized in terms of net heating (including *both* sensible and latent heat)

The heat transfer due to the $\Delta m_t H$ yields an *evaporative* heat transfer coefficient defined through:

$$h^{evap} = \frac{Q_{evap}}{A_s(T_{vapor} - T_a)} = \frac{\Delta m_t H}{(T_{vapor} - T_a)} \tag{3.8}$$

The T_{vapor} is from the measured temperature of *TC1*. In contrast to h^{conv} – see Table 3.2, the h^{evap} is larger with increasing E content and is a measure of the mass loss due to the evaporation. The h^{conv} is then to be interpreted in terms of the heat localization *internal* to the CF and consequent heat loss to the ambient from the bare/CF based surface, while h^{evap} is related to the vapor produced due to the evaporation *external* to the surface. Consequently, there is much less variation in the h^{evap} with and without the CF – indeed, it could even be smaller in the foam due to restricted convection processes, or enhanced viscosity of the *E-W* mixtures, as indicated in Table 3.1.

Table 3.2: Comparison of evaporative heat transfer coefficient (h^{evap}) : defined per Eqn. (3.8), and convective heat transfer coefficient (h^{conv}) : defined per Eqn. (3.7), of water and *E-W* mixtures, with and without the CF based porous medium.

	h^{evap}(W/m^{2}K)	h^{conv}(W/m^{2}K)
Water	31	47
12.5 % E	49	33
25 % E	60	23
37.5 % E	72	15
CF + Water	38	420
CF + 12.5 % E	43	156
CF + 25 % E	47	78
CF + 37.5 % E	57	62

3.4 Conclusion

In summary, we have shown enhanced evaporation of ethanol-water mixtures through the use of CF based porous media. The interplay of heat localization, resulting in a temperature increase, as well as parameters such as the vapor pressure, density, surface tension, and viscosity were carefully considered for understanding the evaporation rate of the mixtures. An increased evaporation rate for the ethanol-water and other binary liquid mixtures could find many applications, ranging from phase separation [3] to distillation [24] and desalination [25].

Chapter 3, in full, has been published in "Enhanced solar thermal evaporation of ethanol-water mixtures through the use of porous media", ACS Langmuir 34, 36, 10523-10528 (2018) by M. Fatih Canbazoglu, B. Fan, K. Vemuri, and P.R. Bandaru. The dissertation author was the primary researcher and author of this material.

3.5 Appendix

A1. Materials and Experimental Systems

Properties of pure components

Table A3.1: Physical properties of pure water and ethanol at 24°C [26-32]

Physical Properties	water	Ethanol
ρ (kg/m^3)	997.2	786.1
C (kJ/kg $^\circ$K)	4.18	2.43
H (kJ/kg)	2444.4	1026.4
$T_{boiling}$ ($^\circ$C)	100	78.4
κ (w/m $^\circ$K)	0.605	0.178
σ (10^{-3} N/m)	72.14	22.44
μ (10^{-3} Ns/m^2)	0.91	1.10
P_v (kPa)	2.97	7.39

Carbon: [33]
ρ=2250 (kg/m^3)
C=0.71 (kJ/kg $^\circ$K)

Properties of Ethanol-Water (*E-W*) Mixtures

Table A3.2: The *E-W* mixtures used in the experiments

Volume ratio of Ethanol	Mass ratio of Ethanol	Mole Fraction
12.5%	10.1%	x_E= 0.043 x_W=0.957
25%	20.8%	x_E= 0.094 x_W=0.906
37.5%	32.1%	x_E= 0.158 x_W=0.842

From the mass ratio of ethanol (*E*) and water (*W*) components, the averaged specific heat (C_{avg}) and density (ρ_{avg}) was estimated for the *E-W* mixture. In the presence of the carbon foam (CF), the 3% solid volume fraction was taken into account, for estimation of C_{avg} and ρ_{avg}. These values were also used for estimating heat transfer coefficient values of the solutions with/without the CF.

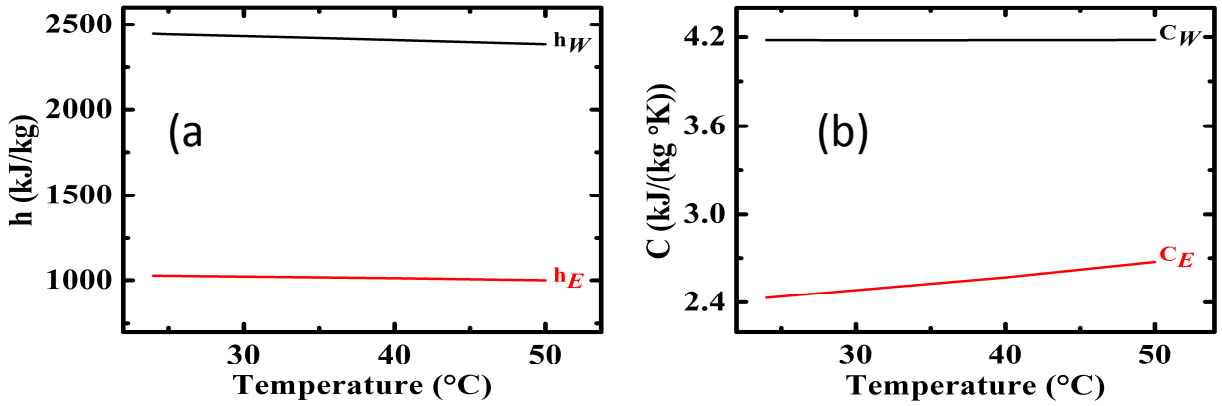

Figure A3.1: Temperature variation of (a) latent heat, and (b) specific heat for water and ethanol [26-32].

Table A3.3: Averaged specific heat capacity (C_{avg}) and density (ρ_{avg}) of the *E-W* mixtures, with and without the CF

Volume ratio of Ethanol	C_{avg}(kJ/kg K)	ρ_{avg}(kg/m^3)
12.5%	4.01	973.6
25%	3.82	947.3
37.5%	3.63	920.9
CF+12.5%	3.79	1012
CF+25%	3.61	986.3
CF+37.5%	3.42	960.8

A2. Estimation of the activity coefficients

The Gibbs free energy of a binary solution (G^E) is represented through:

$$G_E = -RT[x_E ln(x_E + \Lambda_{E-W} x_W) + x_W ln(x_W + \Lambda_{W-E} x_E)] \quad \text{(A2.1)}$$

Here, R is the gas constant, and x_E and x_W are the mole fractions of the components.

The activity coefficients are derived from the Wilson equations [34], as follows:

$$\ln(\gamma_E) = -ln(x_E + \Lambda_{E-W} x_W) + x_W \left(\frac{\Lambda_{E-W}}{x_E + x_W \Lambda_{E-W}} - \frac{\Lambda_{W-E}}{x_W + x_E \Lambda_{W-E}} \right) \quad \text{(A2.2)}$$

$$\ln(\gamma_W) = -ln(x_W + \Lambda_{W-E} x_E) - x_E \left(\frac{\Lambda_{E-W}}{x_E + x_W \Lambda_{E-W}} - \frac{\Lambda_{W-E}}{x_W + x_E \Lambda_{W-E}} \right) \quad \text{(A2.3)}$$

The two adjustable parameters (van Laar Constants), Λ_{E-W} and Λ_{W-E} are related to the pure-component molar volumes and to characteristic energy differences by:

$$\Lambda_{E-W} = \frac{V_{m,W}}{V_{m,E}} exp\left(-\frac{\lambda_{E-W} - \lambda_{E-E}}{RT}\right) \quad \text{(A2.4)}$$

$$\Lambda_{W-E} = \frac{V_{m,E}}{V_{m,W}} exp\left(-\frac{\lambda_{W-E} - \lambda_{W-W}}{RT}\right) \quad \text{(A2.5)}$$

where V_m (cm^3/mol) is a molar volume, $\lambda_{E-W} - \lambda_{E-E}$ (cal/mol) is the interaction energy, *i.e.,* ($\lambda_{E-W} - \lambda_{E-E}$ = 325.08 cal/mol, $\lambda_{W-E} - \lambda_{W-W}$ = 953.28 cal/mol).

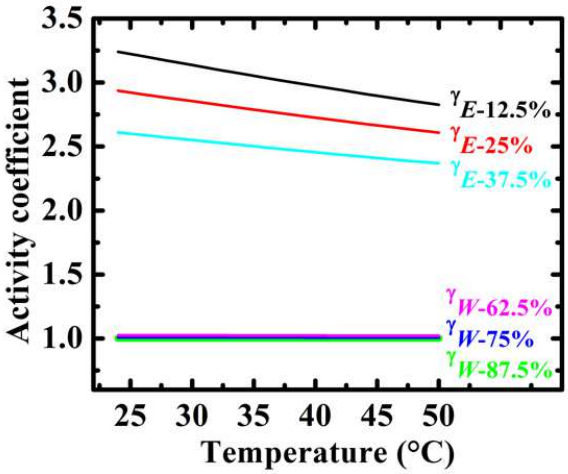

Figure A3.2: The variation of the activity coefficients for ethanol (E)-water (W) mixtures. Generally, as the *E* concentration and/or the temperature increases, there is a decrease in the activity coefficient.

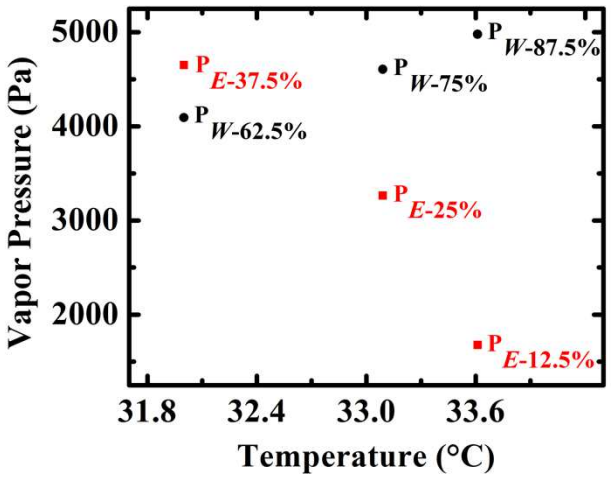

Figure A3.3: The variation, with temperature, of the partial pressure for ethanol (E)-water (W) mixtures. The vapor pressure (related to the volatility or tendency for evaporation [35]) is largest for higher *E* concentrations.

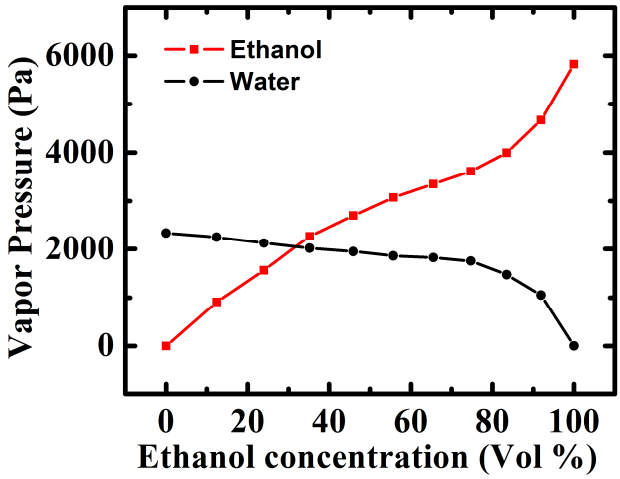

Figure A3.4: The variation, with ethanol concentration, of the vapor pressure for ethanol (E)-water (W) mixtures. (at 20°C) [36]

A3. Evaluation of the evaporative characteristics of *E-W* mixtures

The relative variation, as a function of *T* is understood through:

$$\frac{d(\Delta m_t)}{\Delta m_t} = Z\left(\frac{3}{2}\frac{dP_v}{P_v} + 2\frac{d\mu}{\mu} - 2\frac{d\sigma}{\sigma} - \frac{1}{2}\frac{d\rho}{\rho}\right) \tag{A3.1}$$

The $\frac{d(\Delta m_t)}{\Delta m_t}$ was estimated, from the experimental mass change curves – from Figure 3.2(a), through consideration of the change of the considered parameters, *i.e.,* P_v, μ,σ, ρ as a function of temperature. The discretization was done at two values of temperatures: T_1 and T_2, related to two different values of the time: t_1 and t_2, and with a temperature interval of 2 degrees K, *i.e.,* $T_2\ (t_2) = T_1(t_1) + 2$. Consequently, at two points, say 1 = (T_1, t_1) and 2 = (T_2, t_2), the variation of mass change is parameterized through:

$$\frac{d(\Delta m_t)}{\Delta m_t} = \frac{(\Delta m_t)_2 - (\Delta m_t)_1}{(\Delta m_t)_1} \tag{A3.2}$$

Considering, for example, two values of time 60 s apart, we obtain:

$$\frac{d(\Delta m_t)}{\Delta m_t} = \frac{\frac{m_{2,(t2+60)} - m_{2,(t_2)}}{60} - \frac{m_{1,(t1+60)} - m_{1,(t_1)}}{60}}{\frac{m_{1,(t1+60)} - m_{1,(t_1)}}{60}} = \frac{(m_{2,(t2+60)} - m_{2,(t_2)}) - (m_{1,(t1+60)} - m_{1,(t_1)})}{(m_{1,(t1+60)} - m_{1,(t_1)})}$$

$$\begin{gathered}
\frac{d\mu}{\mu} = \frac{\mu_{T_2} - \mu_{T_1}}{\mu_{T_1}} \\
\frac{d\sigma}{\sigma} = \frac{\sigma_{T_2} - \sigma_{T_1}}{\sigma_{T_1}} \\
\frac{dP_{vap}}{P_{vap}} = \frac{P_{vap_{T_2}} - P_{vap_{T_1}}}{P_{vap_{T_1}}} \\
\frac{d\rho}{\rho} = \frac{\rho_{T_2} - \rho_{T_1}}{\rho_{T_1}}
\end{gathered} \tag{A3.3}$$

The relative variation of the considered physical parameters with temperature, for the estimates in is indicated below:

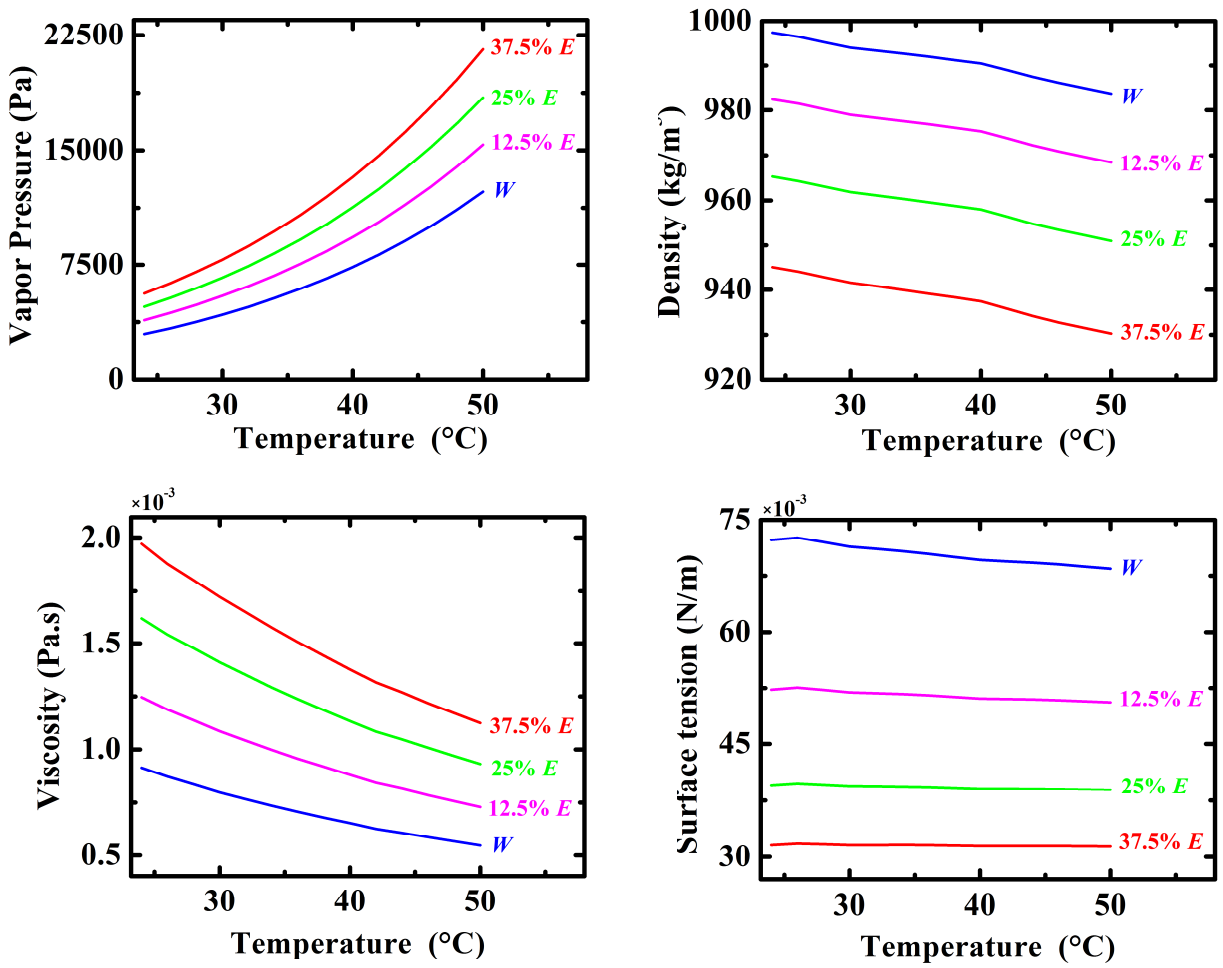

Figure A3.5: The influence of factors affecting the evaporation of ethanol-water mixtures, including **(a)** vapor pressure (P_v), **(b)** density (ρ), and **(c)** surface tension (σ), and **(d)** viscosity (μ),as a function of temperature with correspondence to Figure 3.3, of the main text.

The corresponding *Z* factor was estimated and is indicated in Table A3.1 below:

Table A3.4: The estimated values of the *Z* of *E*-*W* solution mixtures

	$Z_{average}$
Water	-1.24
12.5% E	-0.87
25% E	-1.27
37.5% E	-1.03
CF + Water	-0.60
CF + 12.5% E	-0.79
CF + 25% E	-0.88
CF + 37.5% E	-0.69

The close correspondence of Z to unity indicates that the mass loss rate, as a function of temperature, is quite accurately captured by the P_v, μ, σ, and ρ variation. The $Z_{average}$ value of solutions with CF is smaller, due to the greater temperature increase, and a smaller $\frac{d(\Delta m_t)}{\Delta m_t}$ value. It is relevant to note that $Z_{average}$ for 37.5 % ethanol solution is close to unity, considering the widest time range (1039.9 – 3550.1 seconds) between 28°C-32°C.

Table A3.5: The relative contribution of the physical parameters on the $\frac{d(\Delta m_t)}{\Delta m_t}$ of *E-W* mixtures

	P_v %	μ %	σ %	ρ %
Water	65.79	30.08	3.97	0.16
12.5% E	65.09	31.65	3.09	0.17
25% E	65.15	32.70	1.96	0.19
37.5% E	65.55	33.18	1.07	0.20

It is clear that vapor pressure (P_v) and viscosity (μ) have the largest impact (~97%) on the total evaporation rate while surface tension (σ) and density (ρ) seem to be much less significant.

A4. The convective and evaporative heat transfer coefficient calculations

Estimation of the convective heat transfer coefficient:

The Temperature-time profiles depicted in Figure 3.2(b) were fitted per the following equation:

$$\frac{T(t)-T_a}{T_i-T_a} = \exp\left(-\frac{h^{conv}A_s}{\rho VC}\ t\right) \qquad \text{(A4.1)}$$

The data fits are indicated below:

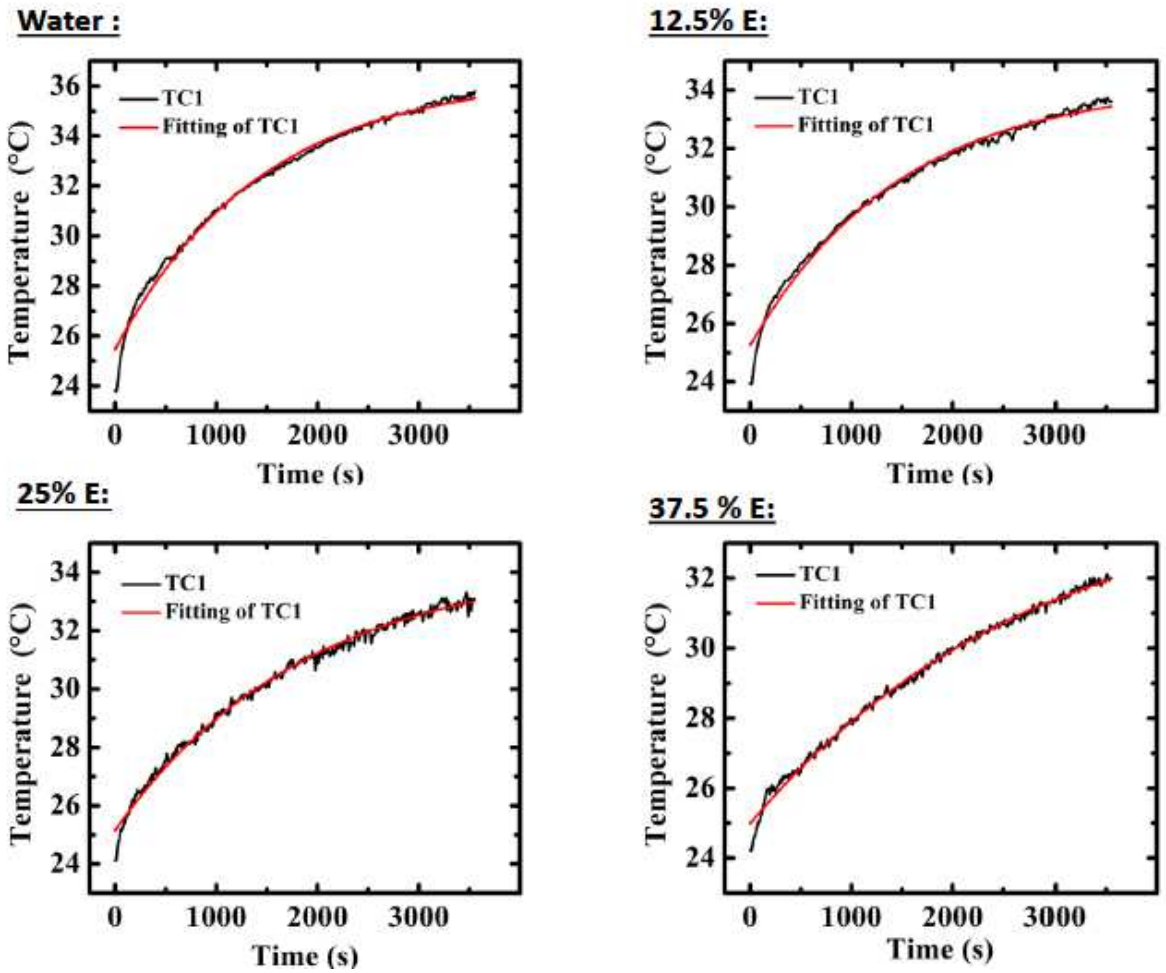

Figure A3.6: The Temperature-time plots related to the evaporative characteristics of water and *E-W* mixtures – in the absence of CF, related to Figure 3.2(b), and the corresponding fits per Eqn. A4.1.

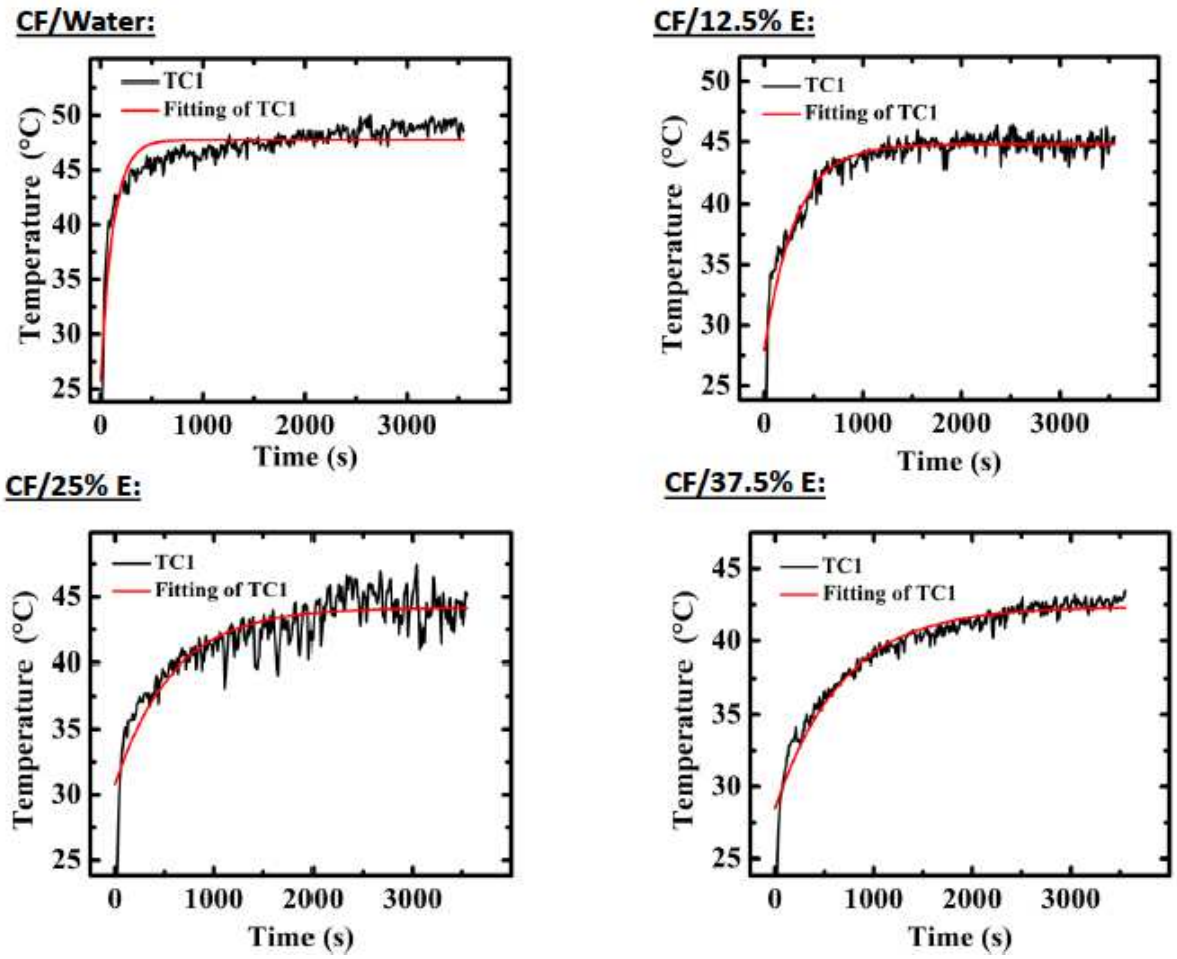

Figure A3.7: The Temperature-time plots related to the evaporative characteristics of water and *E-W* mixtures – in the presence of CF, related to Figure 3.2(b), and the corresponding fits per Eqn. A4.1.

Table A3.6: Experimentally observed R $(= \frac{h^{conv} A_s}{\rho V C})$ and the derived heat transfer coefficient h^{conv} of water and *E-W* mixtures with/without CF. TC1-TC5 corresponds the temperature difference between the top surface and bottom part of the *E-W* mixture.

	R (10^{-4})	h^{conv}(W/m^{2}K)	TC1-TC5 (°K)
Water	9.3	47	3.4
12.5% *E*	6.7	33	2.1
25% *E*	5.36	23	1.5
37.5% *E*	3.53	15	0.9
CF + Water	83	420	24.3
CF + 12.5% *E*	32.1	156	20.5
CF + 25% *E*	17.2	78	19.7
CF + 37.5% *E*	14.8	62	17.4

It was observed that when ethanol concentration increases, that the temperature difference between the top and bottom of the mixture, *i.e.,* the difference |TC1-TC5| decreases. This may occur due to (a) a diminished convection due to the reduced h^{conv}, as well as (ii) a reduced thermal conductivity of the mixture, as the thermal conductivity of ethanol (~ 0.2 W/mK) is less than that of water (~ 0.6 W/mK).

Estimation of the evaporative heat transfer coefficient:

The evaporative heat transfer coefficient (h^{evap}) was estimated from:

$$h^{evap} = \frac{Q_{evap}}{A_s(T_{vapor}-T_a)} = \frac{\Delta m_t H}{(T_{vapor}-T_a)} \quad \text{(A4.2)}$$

Table A3.7: Comparison of evaporative heat transfer coefficient (h^{evap}): Eqn. (A4.2) and convective heat transfer coefficient (h^{conv}) : Eqn. (A4.1) of water and *E-W* mixtures, with and without the CF

	h^{evap}(W/m^{2}K)	h^{conv}(W/m^{2}K)
Water	31	47
12.5% E	49	33
25% E	60	23
37.5% E	72	15
CF + Water	38	420
CF + 12.5% E	43	156
CF + 25% E	47	78
CF + 37.5% E	57	62

It is quite interesting to see that as ethanol concentration increases, that the h^{evap} value increases while h^{conv} value decreases. The h^{evap} is related to the vapor produced due to the evaporation *external* to the CF, while the h^{conv} may be interpreted in terms of the heat localization *internal* to the CF and consequent heat loss to the ambient. In spite of a higher evaporation, through mass loss – see Figure 3.2(a) in the main text, through the use of the CF, h^{evap} through the use of the CF may then be less compared to the values obtained without the CF, due to the greater magnitude of the ($T_{vapor} - T_a$) values.

3.6 References

[1] F.M. Canbazoglu, B. Fan, A. Kargar, K. Vemuri, and P.R. Bandaru, AIP Adv. **6**, (2016).

[2] H. Ghasemi, G. Ni, A.M. Marconnet, J. Loomis, S. Yerci, N. Miljkovic, and G. Chen, Nat. Commun. **5**, 4449 (2014).

[3] O. Neumann, A.D. Neumann, E. Silva, C. Ayala-Orozco, S. Tian, P. Nordlander, and N.J. Halas, Nano Lett. **15**, 7880 (2015).

[4] P.D. Dongare, A. Alabastri, S. Pedersen, K.R. Zodrow, N.J. Hogan, O. Neumann, J. Wu, T. Wang, A. Deshmukh, M. Elimelech, Q. Li, P. Nordlander, and N.J. Halas, Proc. Natl. Acad. Sci. **114**, 6936 (2017).

[5] W.H. Carrier, Ind. Eng. Chem. **12**, 432 (1921).

[6] T.B. Hine, Phys. Rev. **24**, 79 (1924).

[7] R.W. Powell and E. Griffiths, Trans. Inst. Chem. Eng. **13**, 175 (1935).

[8] M. Lurie and N. Michailoff, Ind. Eng. Chem. **28**, 345 (1936).

[9] S.H. Wade, Trans. Inst. Chem. Eng. **20**, 1 (1942).

[10] L.J. O'Brien and L.F. Stutzman, Ind. Eng. Chem. **42**, 1181 (1950).

[11] B.M. Smolsky and G.T. Sergeyev, Int. J. Heat Mass Transf. **5**, 1011 (1962).

[12] K. Asano and S. Fujita, Chem. Eng. Sci. **26**, 1187 (1971).

[13] P.L. Spedding, J. Grimshaw, and K.D. O'Hare, Langmuir **9**, 1408 (1993).

[14] J.E. Brady, General Chemistry: Principles & Structure, 5th ed. (John Wiley & Sons, Jamaica, NY, 1990).

[15] L. Pauling, General Chemistry (Dover Publications Inc., New York, 1969).

[16] M. Potash and P.. Wayner, Int. J. Heat Mass Transf. **15**, 1851 (1972).

[17] P.K. Kundu and I.M. Cohen, Fluid Mechanics, 4th ed. (Academic Press, San Diego, CA, 2008).

[18] R.C. Reid, J.M. Prausnitz, and T.K. Sherwood, Properties of Gases and Liquids, 3rd ed. (McGraw Hill, New York, NY, 1977).

[19] R.V. Orye and J.M. Prausnitz, Ind. Eng. Chem. **57**, 18 (1965).

[20] I.S. Khattab, F. Bandarkar, M.A.A. Fakhree, and A. Jouyban, Korean J. Chem. Eng. **29**, 812 (2012).

[21] T.L. Bergman, A.S. Lavine, F.P. Incropera, and D.P. Dewitt, Introduction to Heat Transfer (John Wiley Inc., Hoboken, NJ, 2011).

[22] A.E. Bergles, J. Heat Transfer **110**, 1082 (1988).

[23] L. Burmeister, Convective Heat Transfer, 2nd ed. (John Wiley & Sons Inc., New York, NY, 1993).

[24] K. Sampathkumar, T.V. Arjunan, P. Pitchandi, and P. Senthilkumar, Renew. Sustain. Energy Rev. **14**, 1503 (2010).

[25] H. Zheng, Solar Energy Desalination Technology, 1st ed. (Elsevier, New York, NY, 2017).

[26] Y. A. Cengel, Heat and Mass Transfer, 3rd ed. (McGraw Hill Inc., New York, NY, 2006)

[27] P. Dunn and D.A. Reay, Heat Pipes, 3rd ed. (Pergamon Press Inc., New York, NY, 1982)

[28] A. Faghri, Y. Zhang, J. Howell, Advanced Heat and Mass Transfer, 1st ed. (Global Digital Press, Columbia, MO 2010)

[29] A. Faghri, Y. Zhang, Transport Phenomena in Multiphase Systems, (Elsevier Academic Press, Burlington, MA, 2006)

[30] M.N. Ivanovskii, V.P. Sorokin, and I.V. Yagodkin, The Physical Principles of Heat Pipes (Clarendon Press, Oxford, UK. 1982)

[31] W.N. Rohsenow, J.P. Hartnett and E.N. Ganic, Handbook of Heat Transfer Fundamentals, 2nd ed. (McGraw Hill Inc, New York, NY, 1985)

[32] N.B. Vargaftik, Handbook of Physical Properties of Liquids and Gases, 2nd ed. (Hemisphere, Washington, DC 1983)

[33] R. G. Sheppard, D. Morgan, D. M. Mathes and D. J. Bray, Properties and Characteristics of Graphite (Poco Graphite, Inc., Decatur, TX 2001)

[34] R. V. Orye and J. M. Prausnitz, Ind. Eng. Chem., **57**, 18 (1965)

[35] K. D. O'Hare, P. L. Spedding and J. Grimshaw, J. Dev. Chem. Eng. Miner. Process., **1**, 118−128 (1993)

[36] K. D. O'Hare, and P. L. Spedding, Chem. Eng J., **48,** 1-9 (1992)